Post-rendezvous radar properties of comet 67P/CG from the Rosetta Mission: understanding future Earth-based radar observations and the dynamical evolution of comets

Essam Heggy, Elizabeth M. Palmer, Alain Hérique, Wlodek Kofman, M. Ramy El-Maarry

Monthly Notices of the ROYAL ASTRONOMICAL SOCIETY

MNRAS **489,** 1667–1683 (2019) doi:10.1093/mnras/stz2174
Advance Access publication 2019 August 12

Post-rendezvous radar properties of comet 67P/CG from the Rosetta Mission: understanding future Earth-based radar observations and the dynamical evolution of comets

Essam Heggy [1,2]★ Elizabeth M. Palmer [1,3] Alain Hérique [4] Wlodek Kofman[4,5] and M. Ramy El-Maarry[6]

[1]*Ming Hsieh Department of Electrical Engineering, University of Southern California, 3737 Watt Way, Los Angeles, CA 90089, USA*
[2]*NASA Jet Propulsion Laboratory, California Institute of Technology, 4800 Oak Grove Drive, Pasadena, CA 91109, USA*
[3]*Department of Geological and Environmental Sciences, Western Michigan University, 1903 W Michigan Avenue, Kalamazoo, MI 49008-5241, USA*
[4]*Université Grenoble Alpes, CNRS, IPAG, F-38000 Grenoble, France*
[5]*Space Research Centre of Polish Academy of Sciences, Bartycka 18A, PL-00–716 Warsaw, Poland*
[6]*Laboratory for Atmospheric and Space Physics, University of Colorado Boulder, 3665 Discovery Drive, Boulder, CO 80303, USA*

Accepted 2019 July 21. Received 2019 June 26; in original form 2018 April 1

ABSTRACT

Radar observations provide crucial insights into the formation and dynamical evolution of comets. This ability is constrained by our knowledge of the dielectric and textural properties of these small-bodies. Using several observations by Rosetta as well as results from the Earth-based Arecibo radio telescope, we provide an updated and comprehensive dielectric and roughness description of Comet 67P/CG, which can provide new constraints on the radar properties of other nuclei. Furthermore, contrary to previous assumptions of cometary surfaces being dielectrically homogeneous and smooth, we find that cometary surfaces are dielectrically heterogeneous ($\varepsilon_r' \approx 1.6–3.2$), and are rough at *X* - and *S*-band frequencies, which are widely used in characterization of small-bodies. We also investigate the lack of signal broadening in CONSERT observations through the comet head. Our results suggest that primordial building blocks in the subsurface are either absent, smaller than the radar wavelength, or have a weak dielectric contrast ($\Delta\ \varepsilon_r'$). To constrain this ambiguity, we use optical albedo measurements by the OSIRIS camera of the freshly exposed subsurface after the Aswan cliff collapse. We find that the hypothetical subsurface blocks should have $|\Delta\ \varepsilon_r'| \gtrsim 0.15$, setting an upper limit of ~ 1 m on the size of 67P/CG's primordial building blocks if they exist. Our analysis is consistent with a purely thermal origin for the ~ 3 m surface bumps on pit walls and cliff-faces, hypothesized to be high-centred polygons formed from fracturing of the sintered shallow ice-bearing subsurface due to seasonal thermal expansion and contraction. Potential changes in 67P/CG's radar reflectivity at these at *X*- and *S*-bands can be associated with large-scale structural changes of the nucleus rather than small-scale textural ones. Monitoring changes in 67P/CG's radar properties during repeated close-approaches via Earth-based observations can constrain the dynamical evolution of its cometary nucleus.

Key words: techniques: radar astronomy – comets: general – comets: individual: 67P/Churyumov-Gerasimenko.

1 INTRODUCTION

Prior to the Rosetta mission, the structural, textural, and electrical properties of cometary nuclei had largely been unconstrained. Consequently, shape models and textural characteristics of cometary nuclei deduced by Earth-based radar observations (one of the primary sources of small-body observations) have been compromised by several uncertainties, thereby reducing our ability to understand the dynamical formation of comets from their shape and from the size of the aggregates forming them.

The Comet Nucleus Sounding Experiment by Radiowave Transmission aboard Rosetta (CONSERT) provides the first *in-situ* radar probing of Comet 67P/Churyumov-Gerasimenko (hereafter

★ E-mail: heggy@usc.edu

67P/CG), measuring the dielectric properties of the smaller lobe of the comet nucleus and assessing its volumetric heterogeneity (Kofman et al. 1998; Kofman et al. 2015). An accurate understanding of the dielectric properties of the comet is essential to understanding CONSERT's results in terms of the dust-to-ice ratio within the bulk interior and in terms of the potential composition of cometary dust, and is essential to understanding the potential occurrence and characteristics of 67P/CG's primordial building blocks, which may be preserved as volumetric scatterers in the subsurface (Kofman et al. 2015; Hérique et al. 2016; Ciarletti et al. 2017; Hérique et al. 2019).

Due to comets' infrequent passes by Earth, as well as their characteristically small diameters and low radar albedos, only a few tens of comets have been observed by Earth-based radar to date (Springmann et al. 2017; Benner 2019). Among these, less than half have independent constraints on their dimensions, as well as measurable radar backscatter, that together permit reliable interpretation of a comet's physical properties (Lamy, Hérique & Toth 2015). Physical properties nominally inferred from radar backscatter measurements include the shape, size, and spin of a comet nucleus (e.g. Harmon et al. 2004). In addition, the power and polarization of the radar return constrain the characteristics of the surface roughness at the scale of the radar wavelength (cm to m), and the complex relative permittivity (i.e. the complex dielectric constant $\varepsilon_r = \varepsilon_r' + i\varepsilon_r''$) of the material that comprises the upper metres of the shallow subsurface (e.g. Harmon et al. 2004; Palmer, Heggy & Kofman 2017). In turn, the dielectric constant of a material at a given radar frequency depends primarily on its mineralogy, bulk density, volatile content, and temperature (e.g. Heggy et al. 2012; Hérique et al. 2016). Hence, while the shape, size, and spin of small-bodies can be constrained by some Earth-based optical and infrared observations, deducing the textural, structural, and dielectric properties of small-bodies generally requires radar observations, whether Earth-based or orbital (e.g. Benner et al. 2008; Kofman et al. 2015; Virkki & Muinonen 2016; Palmer et al. 2017).

Prior to Rosetta's rendezvous with 67P/CG, interpretation of radar backscatter from comet nuclei relied on the assumption that surface scattering can be approximated by geometric optics, in which specular reflections come from each facet surface element, thus enabling estimation of the real part of the surface's dielectric constant ε_r' (e.g. Harmon et al. 2004; Kamoun et al. 2014; Lamy et al. 2015). Under this assumption, previous radar studies of comets have interpreted the low radar reflectivity of the nucleus surface as indicative of a thick layer of porous material at the nucleus surface (e.g. Kossacki & Szutowicz 2008; Rosenberg & Prialnik 2009; Brouet et al. 2014), and that the density of the shallow substrate (underlying the porous layer) can be used as an estimate for the bulk density of the nucleus (e.g. Kamoun et al. 2014), as is postulated for the case of minimal compaction by slow-velocity impactors (Belton et al. 2007).

In support of data inversion for the CONSERT experiment before Rosetta arrived at Comet 67P/CG, we previously developed hypothetical 3D dielectric models of 67P/CG's nucleus that are based on the assumptions above (see Heggy et al. 2012). Rosetta's high-resolution orbital and lander observations now urge the development of updated structural and dielectric models of the comet nucleus – establishing 67P/CG as a reference comet in terms of well-defined radar properties. In Section 2, we review post-rendezvous knowledge of 67P/CG's structure and surface texture to generate a simplified model of the primary surface and subsurface layers of the nucleus. In Section 3, we review post-rendezvous constraints on the primary geophysical properties on which the dielectric constant depends – bulk composition, porosity, ice content, and temperature – for each of the primary nucleus layers defined in Section 2.

In Section 4, we use the results of Sections 2 and 3 to develop an updated 3D post-rendezvous dielectric model of 67P/CG's nucleus. Dielectric modelling of the surface and shallow subsurface is applicable to high-frequency Earth-based radar observations (GHz range), while that of the deeper subsurface is relevant to the low-frequency radar observations (MHz range) that propagate tens to hundreds of metres through the comet's subsurface.

In Section 5, we set an upper limit on the size of the primordial cometary building blocks of 67P/CG by estimating the dielectric contrast of subsurface blocks from albedo contrast measured by OSIRIS and using the constraint that CONSERT has not detected measurable volume scattering at 90 MHz. We discuss the implications of this result for the observed bumpy surface texture of the Seth 01 pit walls in Section 6.

In Section 7, we discuss implications of the updated dielectric model for future Earth-based radar observations of 67P/CG and other cometary nuclei in terms of their structural evolution – such as increasing dust coverage and subsequent smoothening, which have been associated with the decrease in outgassing activity as the result of insolation and surface maturation (e.g. Birch et al. 2017; El-Maarry et al. 2017). The dielectric properties of the nucleus interior, in turn, provides a reference for comparison with future orbital radar sounding observations of cometary nuclei and for Earth-based radar observations in the case of nucleus breakup and subsequent exposure of the interior.

2 POST-RENDEZVOUS STATE OF KNOWLEDGE ON THE STRUCTURE AND TEXTURE OF 67P/CG

The bulk shape of the comet nucleus is shown in Fig. 1(a), consisting of a large lobe (hereafter referred to as the 'body' of the comet), a smaller lobe (the 'head'), and an adjoining region (the 'neck'). In turn, the surface and shallow subsurface of the nucleus has been classified into two primary terrain types (Fig. 1a). There are smooth, loose, fine-grained deposits of dust and ice (Mottola et al. 2015) – where we define 'fine-grained' as blocks smaller than a metre in diameter – and there is rough, consolidated material inferred to be a layer of sintered dust and ice that is exposed where the fine-grained deposits are thin (Pommerol et al. 2015; Spohn et al. 2015). In 67P/CG's northern hemisphere, thick fine-grained dust-ice deposits are most prevalent in the following morphological regions: Ash (located on the body), Hapi (on the neck), and Ma'at (on the head) as defined by El-Maarry et al. (2015a) (and summarized in Table 2 therein). In contrast, thick fine-grained deposits are largely absent from 67P/CG's southern hemisphere (El-Maarry et al. 2016).

Additionally, horizontal strata exposed along outcrops and cliff walls suggest that the upper few hundred metres of the subsurface consist of several layers that are each a few tens of centimetres in thickness to a few metres (Massironi et al. 2015), although the homogeneity or heterogeneity of the dust-to-ice ratio and porosity within the deep subsurface remains a subject of debate (e.g. Davidsson et al. 2016). In Fig. 1, we provide a hypothetical model of the comet's basic surface and subsurface layers that are considered in this study – i.e. thick fine-grained deposits, consolidated material, and the primordial interior. Fig. 1(b) depicts the two primary types of surface terrain, and Figs 1(c) and (d) depict two structural hypotheses for the nucleus interior. In Fig. 2, we show high-resolution images of the two surface terrain types at centimetre

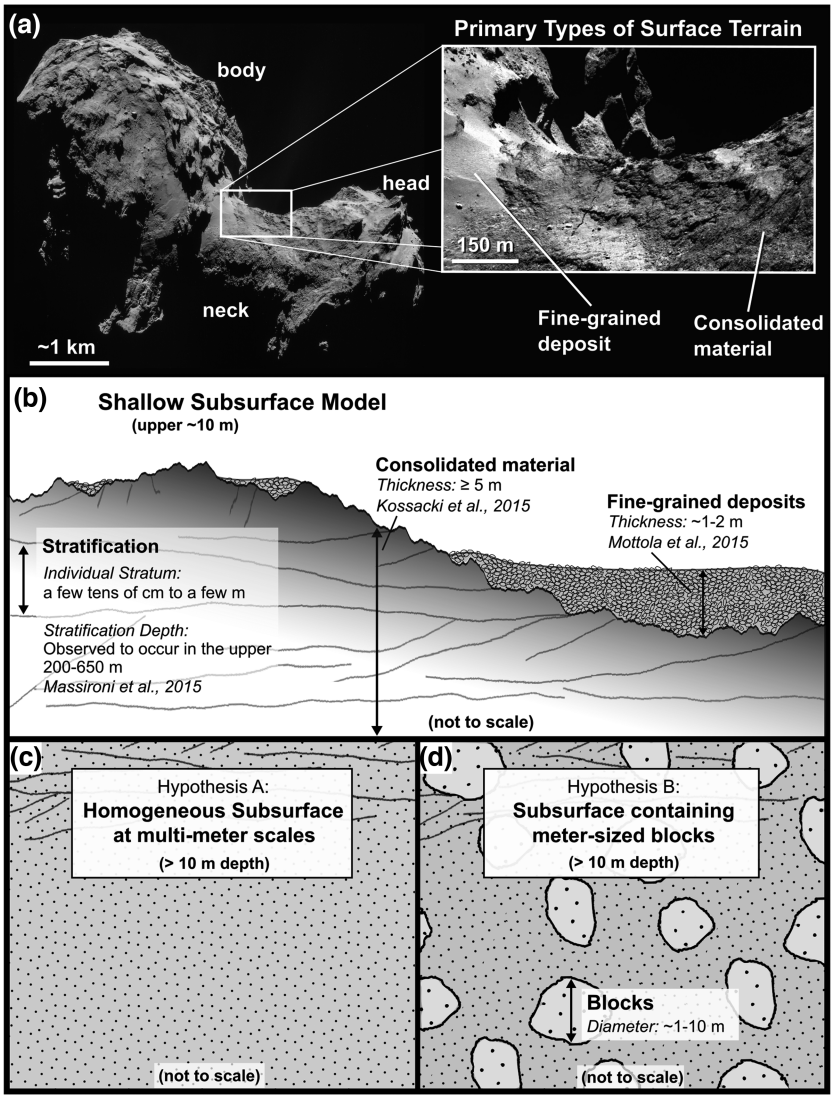

Figure 1. Simplified schematic of the primary surface and subsurface layers used for post-rendezvous dielectric modelling of Comet 67P/CG's nucleus. Thick fine-grained deposits cover ∼30 per cent of the surface and consist of cm-dm-sized fragments that overlay a consolidated layer of sintered dust and ice that is exposed over ∼70 per cent of the surface. We consider two structural models of the bulk interior (∼10–300 m depth): Hypothesis A, homogeneous at multimetre scales, and Hypothesis B, containing ice-rich multimetre-sized primordial building blocks embedded in a dusty matrix.

to metre scales to visualize their textural properties at the *X*-band (8.4 GHz), *S*-band (2.4 GHz), and VHF (90 MHz) frequencies that are used for cometary radar observations.

2.1 Structure and texture of the primary surface and shallow subsurface layers

Surface observations by the Rosetta mission suggest that comets are not uniformly smooth, nor uniformly covered by a thick, porous layer of fine dust such on the Moon (Fig. 1a). Furthermore, unlike asteroid regoliths, the presence of water-ice in the upper metres of the nucleus does not lead to surface smoothening at centimetre-to-decimetre (cm-dm) scales (e.g. Palmer et al. 2017). In particular, the smoothest areas of 67P/CG's nucleus – covering about one-third of the nucleus surface (Birch et al. 2017) – appear to be gravitational lows where loose, fine-grained deposits have accumulated to depths of ∼1–2 m by airfall after outbursts or overhang collapses (Mottola et al. 2015; Thomas et al. 2015; Pajola et al. 2017). However, images from the initial descent of the Philae lander by ROLIS (the Rosetta Lander Imaging System; Mottola et al. 2015) and CIVA (Comet Infrared and Visible Analyser; Bibring et al. 2015), in addition to final descent images by OSIRIS aboard the Rosetta orbiter (Keller et al. 2007), indicate that fine-grained deposits are indeed smooth at multimetre scales (Fig. 2a), but appear to have a rough, granular texture at cm-dm scales (Figs 2b and c).

Terrains consisting of consolidated material, in contrast, are much harder and less porous than fine-grained deposits, and are rough at all scales applicable to radar observations – from decametres down to cm (Figs 2d–f). Consolidated material dominates the surface texture of 67P/CG since it is exposed over at least two-thirds of the nucleus surface (Birch et al. 2017). Furthermore, OSIRIS imagery of the walls of deep sinkholes, cliffs, and outcrops shows that consolidated material is prone to thermal stress fractures from rapid diurnal and long-term seasonal effects of heating and cooling (e.g. El-Maarry et al. 2015b; Vincent et al. 2015; Auger et al. 2018). Kossacki et al. (2015) modelled the sintering process as a function of

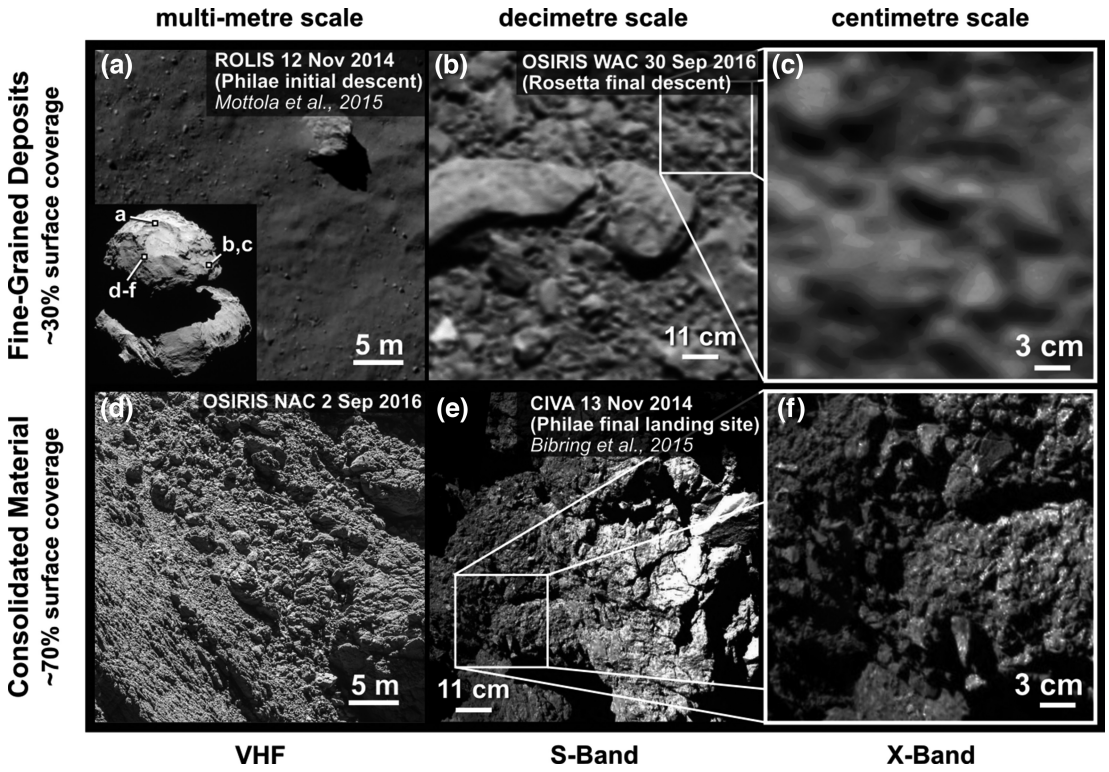

Figure 2. The surface of Comet 67P's nucleus can be classified into two primary terrain types (e.g. El-Maarry et al. 2015a) – thick fine-grained dust-ice deposits of loose blocks ∼1 m, and exposures of underlying consolidated material. The six above images from ROLIS, CIVA, and OSIRIS provide a comparison of surface roughness at different scales between the two terrain types. Fine-grained deposits appear smooth at multimetre scales but contain scattered fragments at decimetre scales and appear rough (speckled, granular) at cm-dm scales. Consolidated material is rough at all scales relevant to radar observations – from cm to tens of metres.

ice grain size in the upper layers of the nucleus and the increasing thickness with time, and find that this sintered dust-ice layer has grown at least 1–5 m thick over the considered time period (1959–2015, 8.5 orbits).

2.2 Quantifying surface roughness

Given the apparent variability of surface roughness over the comet nucleus – at different scales of interest for radar observations (Fig. 2) – the accurate inversion of 67P/CG's dielectric properties from Earth-based and orbital radar observations will be highly dependent on accurate quantification of surface texture as is directly addressed by the work of Birch et al. (2017). Birch et al. (2017), use 2D photoclinometry to derive decimetre-resolution digital terrain models from the shadows observed in high-resolution OSIRIS images, and apply this technique to six different types of geomorphologies on 67P/CG – pitted plains, cauliflower plains, smooth plains, talus deposits, cliffs, bouldered plains, and mottled pit terrains – from which they calculate surface slopes (over 14 cm baselines) and root-mean-square height $h_{\rm rms}$. Birch et al. (2017) also measure the cumulative size-frequency distribution of boulders within each surface unit, counting boulders at scales as small as ∼3 cm in diameter in a few selected ROLIS images from the Philae lander's descent to boulders as large as ∼5 m in diameter in high-resolution OSIRIS narrow-angle camera (NAC) images.

Birch et al.'s (2017) analysis confirms that 67P/CG's geomorphological surface units can be quantitatively grouped into (1) smooth terrains – including the smooth plains, pitted plains and cauliflower plains – which are distinguished by surface slopes of ∼4°–13° (over 14 cm baselines) with $h_{\rm rms} < 24$ cm; and (2) rough terrains – including cliffs, talus deposits, bouldered plains, and mottled pit terrains – which are distinguished by surface slopes of 23°–26° (over 14 cm baselines) with $h_{\rm rms} > 50$ cm. It should be noted, however, that the smoothness of different surface units does not always imply greater thickness of the dust layer. For instance, the Hapi region is characterized by smooth plains, but also has the highest measured average water-ice abundance of ∼10–15 per cent among all geologic regions of the surface (excluding exposed ice patches; De Sanctis et al. 2015). Given the variably rough terrain of the nucleus, incorporating Birch et al.'s (2017) surface roughness models of Comet 67P/CG are also necessary for unambiguous inversion of the average dielectric properties of the comet surface from Earth-based radar observations.

2.3 Inner structure of the comet head

The hypothesis for a structurally homogeneous nucleus interior (Hypothesis A, Fig. 1c) has been bolstered by multiple lines of evidence from the Rosetta mission. Even though horizontal strata tens of metres in thickness are unambiguously identified along several outcrops and on cliff walls from OSIRIS imagery – observed to reach depths of ∼200 m, and inferred to continue to depths of ∼650 m; Massironi et al. 2015) – the Rosetta Radio Science Investigation (RSI; Pätzold et al. 2007) finds no heterogeneity in the comet's global density distribution from the comet's gravity field at orbital distances of 10–100 km (Pätzold et al. 2016). In addition, CONSERT did not detect any measurable broadening

of the radar pulse within the comet head (Kofman et al. 2015) – which can be attributed to a lack of volume radar scattering (Kofman et al. 1998; Carley & Heggy 2008; Ciarletti et al. 2017; Hérique et al. 2019) – suggesting that the subsurface is relatively homogeneous in its dielectric properties at multimetre scales, and hence in the subsurface distribution of porosity and dust-to-ice mass ratio (Kofman et al. 2015; Hérique et al. 2019). The case for a homogeneous nucleus is further supported by cometary formation modelling by Blum et al. (2017), who find that Rosetta and Philae's observational constraints on porosity, surface tensile strength, and subsurface temperatures are consistent with the formation of Comet 67P/CG by slow gravitational accumulation of mm-sized dust aggregates ('pebbles') interspersed with icy grains, resulting in a homogeneous nucleus at all scales down to the pebble size.

The possibility of multimetre-scale heterogeneity in the subsurface, however (Hypothesis B, Fig. 1d), has been suggested in light of geomorphological evidence for differential sublimation along the walls of active pits as observed by OSIRIS (Sierks et al. 2015; Davidsson et al. 2016) and also when considering the uneven distribution of large pits that are tens to hundreds of metres in depth and are thought to have formed by the collapsing of material over large subsurface cavities (Vincent et al. 2015). The surface texture that may be indicative of differential sublimation has been observed on several steep slopes, such as cliff-sides and along the walls of sinkholes, and is described by various authors as 'goosebumps' (Sierks et al. 2015), a 'globular' texture (Vincent et al. 2015), or 'clods' and 'lumps' (Davidsson et al. 2016). Davidsson et al. (2016) measured the size-frequency distribution of the surface bumps in three different regions on 67P/CG and found that their characteristic diameters are $\sim 2.5 \pm 1$ m, roughly equal to the radar wavelength of CONSERT's observations ($\sim$3 m in vacuum). It is argued that the individual bumps may in turn represent the characteristic size of primordial building blocks from the formation of the comet (Sierks et al. 2015; Davidsson et al. 2016). Hereon, we refer to the nodular features as 'surface bumps' or as the 'bumpy surface texture.'

The argument for a heterogeneous nucleus interior has also been supported by Jorda et al. (2016) and Gutiérrez et al. (2016), who suggest that even if the density of one lobe of the comet is greater than the other, structurally homogeneous interiors are insufficient to explain the calculated coordinates of the centre-of-mass, as well as the measured precession of the spin axis.

The aforementioned lack of volume scattering in CONSERT observations, however, places limits on the size and dielectric contrast of potential primordial blocks within the nucleus interior. We will present dielectric modelling of a homogeneous interior in Section 4, and in Section 5 we will present constraints on the dielectric contrast and size of primordial building blocks.

3 POST-RENDEZVOUS STATE OF KNOWLEDGE ON THE GEOPHYSICAL AND DIELECTRIC PROPERTIES OF 67P/CG

In this section, we summarize the updated geophysical and radar observations of 67P/CG by Rosetta and the Arecibo Observatory that will be used to build an updated dielectric model of the nucleus in the next section. We begin by reviewing post-rendezvous knowledge of the comet's major constituent materials: cometary refractory material (hereafter 'dust' for simplicity) and cometary ice. Next, we review post-rendezvous knowledge of the porosity of each of the nucleus' primary surface and subsurface layers (i.e. thick fine-grained deposits, consolidated material, and the primordial interior), and their dust-to-ice ratio.

Finally, we use the results of Earth-based high-frequency *S*-band radar observations of 67P/CG by Arecibo (Kamoun et al. 2014) in combination with the results of Rosetta's low-frequency VHF radar observations (Kofman et al. 2015; Hérique et al. 2016) to constrain the nucleus' 3D distribution of dielectric properties. The geophysical properties constrained below are used as input for updated dielectric modelling of 67P/CG in Section 4.

3.1 Cometary dust: composition, solid density, and dielectric properties

Comet 67P/CG's nucleus is covered by dust with a very low optical albedo that is spectroscopically consistent with refractory, carbonaceous organic material mixed with opaque minerals, such as iron-nickel alloys or iron sulphides (e.g. Quirico et al. 2016; Filacchione et al. 2016a). While previous studies postulated that hydrated carbonaceous chondrites (i.e. such as CI, CR, and CM meteorites types) may constitute the comets' dust, VIRTIS does not detect any hydrated minerals on the nucleus' surface, thereby excluding these meteorite classes from probable dust analogue materials for 67P/CG (Capaccioni et al. 2015; Quirico et al. 2016). In addition, spectroscopic measurements of dust coma particles by Rosetta's Comet Secondary Ion Mass Spectrometer (COSIMA) suggest that 67P/CG's dust component is composed of $\sim$45 wt per cent organic material and $\sim$55 wt per cent anhydrous mineral phases (Bardyn et al. 2017). While the carbon content is high however, Bardyn et al. (2017) find that 67P/CG's dust carbon abundance is much lower than some UltraCarbonaceous Antarctic MicroMeteorites (UCAMMs), which are another proposed analogue for cometary dust material (Dobrică et al. 2012).

Radar observations by CONSERT, in conjunction with constraints on the nucleus' bulk density and dust-to-ice ratio, also rule out ordinary and CM carbonaceous chondrites as major constituents of the dust component, while the lack of hydrated minerals in 67P/CG observed by VIRTIS further rules out the CR2 carbonaceous chondrite. Hérique et al. (2016) conclude that a minimum of 75 per cent volume fraction of organic materials in association with Mg-silicates would be required to satisfy the observed dielectric and density properties of the nucleus interior.

This has direct implications for the previous dielectric models of 67P/CG's nucleus that were constructed using laboratory-measured dielectric properties of ordinary chondrite meteorite powder mixed with water-ice (Heggy et al. 2012). Using CONSERT's and VIRTIS' constraints on the dielectric and spectral properties of cometary dust, respectively, Hérique et al. (2016) instead show that the best compositional analogues to 67P/CG's dust component requires the laboratory synthesis of refractory organic materials with a mixture of opaque minerals and semivolatiles (light-weight materials that are stable below $\sim$220 K, the comet's average surface temperature, but which cannot survive the transit through Earth's atmosphere and are therefore absent from all meteorite samples).

Since we lack comprehensive dielectric measurements of established cometary dust analogue materials at very low temperatures and in vacuum (e.g. Hérique et al. 2002; Heggy et al. 2012; Brouet et al. 2016), we adopt the range of dust permittivity values that are constrained by Hérique et al. (2016), who find that the solid permittivity $\varepsilon_{r}{}'_{(s)dust} \lesssim 5.4$ – where we use the subscript '(s)' for 'solid' to denote zero micro or macro porosity – although this value is stated to be an extreme upper limit, significantly refined in the conclusion of the same paper. To evaluate the effect of the dust component's permittivity on the effective dielectric constant of different parts of the comet, we therefore input six different values

of $\varepsilon_r{}'_{(s)dust}$ that span its possible range (1.5, 2.0, 2.5, 3.5, 4.5, and 5.4) when calculating the effective dielectric constant $\varepsilon_r{}'_{eff}$ of a hypothetical mixture of cometary dust and cometary ice.

Regarding the solid density of cometary dust, Pätzold et al. (2019) find that the material densities employed by Kofman et al. (2015) and Hérique et al. (2016) for CONSERT data analysis – i.e. $\rho_{(s)dust} = 2000–3500\,kg\,m^{-3}$ – are more compatible with the mass and bulk density of 67P/CG that are determined from RSI observations (Pätzold et al. 2016), rather than the lower range of $\rho_{(s)dust} = 1925^{+2030}_{-560}\,kg\,m^{-3}$ estimated by Fulle et al. (2017) using measurements of dust particles' masses and cross-sections in the dust coma by GIADA (the Grain Impact Analyser and Dust Accumulator Aboard Rosetta; Della Corte et al. 2015). In this study, we therefore adopt the range $\rho_{(s)dust} = 2000–3500\,kg\,m^{-3}$.

3.2 Cometary ice: composition, density, and dielectric properties

Water-ice and frozen carbon dioxide have each been identified in VIRTIS spectral images of bright patches exposed on the comet surface (Filacchione et al. 2016b). The comparison of measurements by the Rosetta Ptolemy mass spectrometer (Wright et al. 2007) and those by the Rosetta Orbiter Spectrometer for Ion and Neutral Analysis (ROSINA; Balsiger et al. 2007) of the ratio of carbon-bearing coma volatile species suggest that ice within the comet nucleus is most likely crystalline water-ice in which CO_2 and CO molecules have condensed in the pores of dust-ice mixtures (Brugger et al. 2016). However, amorphous ice has also been postulated to occur at depths below at least a few metres (e.g. Guilbert-Lepoutre et al. 2016; Prialnik & Sierks 2017). To address different possible mixtures of cometary icy volatiles, we adopt two end-members described by Hérique et al. (2016): one theoretical ice mixture with a content of H_2O: CO_2: CO = 94:3:3 per cent (for which $\rho_{(s)ice} = 931–1171\,kg\,m^{-3}$ and $\varepsilon_r{}'_{(s)ice} = 2.7–3.0$), and the other with H_2O: CO_2: CO = 75:8:17 per cent (for which $\rho_{(s)ice} = 945–1138\,kg\,m^{-3}$ and $\varepsilon_r{}'_{(s)ice} = 3.0–3.3$).

3.3 Porosity of fine-grained deposits, consolidated material, and the pristine interior

The bulk porosity of the 1–2 metre-thick fine-grained deposits have not been measured through observations by Rosetta, so we begin with observations of consolidated material. Basilevsky et al. (2016) constrained the consolidated layer's compressive strength based on the pressure exerted by the legs of the Philae lander upon impact with the surface, and by estimating the fragility of cliffs where faces had crumbled, finding that the consolidated layer is much harder than the loose, porous fine-grained dust-ice deposits, and is comparable to the hardness of dry snow (i.e. rigid, porous crystalline water-ice with no residual moisture) at 263 K. Along the same lines, Spohn et al. (2015) estimate that the layer of consolidated material has 40 per cent $< P <$ 55 per cent (or 30 per cent $< P <$ 65 per cent including error bars) given its impenetrability by the Rosetta MUPUS hammer (Multipurpose Sensors for Surface and Sub-Surface Science). Rosetta's permittivity probe experiment SESAME-PP (Surface Electrical Sounding and Acoustic Monitoring Experiments – Permittivity Probe) at Philae's final landing site Agilkia has also found that the electrical properties of the shallow subsurface are consistent with $P < 50$ per cent (Lethuillier et al. 2016).

Next, we estimate the porosity P_{depos} of thick fine-grained deposits on 67P/CG using equation (4) from Kiuchi and Nakamura (2014), which relates the porosity of loosely packed regolith on desiccated airless bodies to the size of the constituent particles (for radii of ∼1 μm to ∼1 m). Input parameters include the minimum porosity possible by random packing p_0 (0.36 or 0.4); surface gravity $g \approx (1.7 \pm 0.5) \times 10^{-4}\,m\,s^{-2}$ (Pajola et al. 2017); the Hamaker constant A, which is related to the strength of the van der Waals force between particles of certain compositions, where $A \approx (3–10) \times 10^{-20}$ J for hydrocarbon crystals in vacuum (e.g. Israelachvili 2011; Thomas et al. 2015); the cleanliness ratio $S \approx 1$ (for particles in low-pressure, high-vacuum conditions); and mean particle radius r. Using rock size distributions derived for fine-grained deposits on 67P/CG by Pajola et al. (2017) from OSIRIS images of Philae's initial descent site (Agilkia) and of Rosetta's final descent site (Sais), we calculate the corresponding cumulative rock size distributions, and find that the mean diameter for each fine-grained deposit is ∼4 and ∼6 cm, respectively, yielding a mean rock radius of $r \approx 2.5$ cm. With these input values, equation (4) from Kiuchi and Nakamoto (2014) yields $P_{depos} \approx 55–70$ per cent.

Regarding the nucleus interior, Pätzold et al. (2016) measure variations in the spacecraft's velocity due to the nucleus' gravity field, and use the volume determined from nucleus shape models (Preusker et al. 2015) to constrain the comet's bulk density to $\rho_{bulk} = 533 \pm 6\,kg\,m^{-3}$. Combining bulk density with CONSERT's measurements of $\varepsilon_r{}'$ of the comet head interior – and ensuing constraints on the dust-to-ice mass ratio (described in Section 3.4) – the comet head interior is suggested to have a bulk porosity between ∼75 and 85 per cent (Kofman et al. 2015; Hérique et al. 2016).

3.4 Dust and ice distribution in fine-grained deposits, consolidated material, and the pristine interior

The comet's surface has a low geometric albedo of ∼0.065 at 649 nm, consistent with the widespread distribution of dark refractive material (e.g. Fornasier et al. 2015). Additionally, several small, bright patches <10 m have been observed by OSIRIS that have been spectrally confirmed as water-ice by VIRTIS (Capaccioni et al. 2015; Pommerol et al. 2015; Sierks et al. 2015). Furthermore, the diurnal and seasonal cycles of water-ice exposure, sublimation, and recondensation on the surface are now well-documented over the course of the two-year Rosetta mission (e.g. De Sanctis et al. 2015; Ciarniello et al. 2016; Oklay et al. 2017).

During the night and during seasonal shadowing, water vapour from the coma recondenses into a thin frost in the upper few microns of the surface that can create icy patches up to ∼1500 m^2 in extent (De Sanctis et al. 2015; Fornasier et al. 2016). On the dayside, surfaces temperatures quickly reach >200 K under direct sunlight, causing the re-sublimation of the thin water-ice cover (Capaccioni et al. 2015; Filacchione et al. 2016b). However, this frost layer is much thinner than the scale of the observing wavelength for orbital VHF (MHz) or Earth-based *X*- and *S*-band (GHz) radar and is therefore excluded from our dielectric modelling of the 67P/CG nucleus.

By contrast, longer surviving exposures of subsurface water-ice have been observed to last days, weeks, months, or years depending on the size and depth of the underlying ice reservoir. Oklay et al. (2017) estimate that one ice exposure (which lasted throughout the entirety of the Rosetta mission) has a high water-ice abundance of ∼48 per cent and covers an approximate surface area of ∼75 m^2 on the Imhotep region (underside of the comet body). Oklay et al. (2017) also observe clusters of ice-rich boulders that each shrink with time via sublimation and are estimated to contain as much as ∼6–25 per cent water-ice; such boulder clusters cover areas of ∼1500 to 15 000 m^2 (∼0.002–0.02 km^2) at the base of cliffs and

taluses. Notably, such small, isolated features will not be resolved within the large footprint of Earth-based radar observations, so the surface will appear to have a uniform ratio of dust-to-ice.

The measured dust-to-gas mass ratio $M_{d/g} = 4 \pm 2$ for Comet 67P/CG is based on a combination of (1) dust coma measurements by OSIRIS and GIADA; and (2) gas-coma measurements by MIRO (Microwave Instrument for the Rosetta Orbiter) and ROSINA (Rotundi et al. 2015). Contrary to initial assumptions that $M_{d/g}$ would closely match the dust-to-ice mass ratio $M_{d/i}$ of the comet's pristine interior, Fulle et al. (2017, 2019) find that $M_{d/g}$ samples the $M_{d/i}$ of fine-grained deposits, which are comprised of chunks of dust and ice that have fallen back onto the nucleus, and that the pristine nucleus interior is at least 10 times more dust-rich – corresponding to depths potentially $\geq$4 m (Fulle et al. 2019) – where $M_{d/i\ (nucleus)} > 3$. Pätzold et al. (2019) find that within the range of $\rho_{(s)dust} = 2000$–$3500\ kg\ m^{-3}$ used in data analysis by both CONSERT and RSI studies (Hérique et al. 2016; Pätzold et al. 2016), $3 \geq M_{d/i\ (nucleus)} \geq 7$ is consistent with the hypothesis of a highly porous dusty body with little ice, whereas higher values of $M_{d/i\ (nucleus)}$ are less likely as they suggest very little to no ice occurrence in the pristine material of the nucleus.

Hereafter, we will refer to the dust-to-ice mass ratio of the consolidated layer and deep interior simply as $M_{d/i}$, and that of the fine-grained deposits as $M_{d/i\ (depos)}$. In Section 4, we use discrete values of $M_{d/i} = 3$, 5, and 7 for pristine material, along with corresponding values of $M_{d/i\ (depos)} = 2$, 4, and 6 for the fine-grained deposits. Without knowing how the vertical profile of $M_{d/i}$ varies in the upper metres of the consolidated material layer, we assume that $M_{d/i}$ of the consolidated material layer is equal to that of the deep interior for simplicity. However, the effects of a higher or lower $M_{d/i}$ on the dielectric constant of individual units can be readily determined from the results of Section 4.

3.5 Observational constraints on the dielectric properties of the comet nucleus

Observations by CONSERT, SESAME-PP, and the Earth-based Arecibo radio telescope have provided constraints on the dielectric properties of 67P/CG over radar frequencies from ~10 to ~10 GHz. In spite of the large range of observation frequencies, the dielectric constant ε_r' of cometary dust – comprised of porous, desiccated carbon-rich organics – is expected to be non-dispersive over this frequency range as shown by dielectric measurements of analogue materials such as bitumen from 1 kHz to 1 GHz by von Hippel (1995), and as catalogued for other organics in the MHz-GHz range by Hérique et al. (2016; table A2 therein). Furthermore, given the low temperatures of the cometary environment – reaching a maximum of 220–230 K at 67P/CG's surface (Tosi et al. 2015) and a minimum potentially as low as 25–50 K in the nucleus interior (Choukroun et al. 2015) – the ε_r' of cometary ices (e.g. crystalline or amorphous water-ice) are also expected to be non-dispersive over the range of kHz-GHz (Hérique et al. 2016; and references therein). However, Lethuillier et al. (2016) point out that at the above maximum surface temperatures, $\varepsilon_{r\ water\text{-}ice}'$ is larger at frequencies <1 kHz when compared to the MHz-GHz range (see the first figure by Lethuillier et al. 2016). Hence, for a given mixture of cometary dust and ice, we will consider SESAME-PP's dielectric measurements in the Hz-kHz frequency range to represent upper limits of ε_r' when we construct our dielectric model in Section 4 for VHF and *X*- and *S*-band radar observations.

Regarding observational constraints on the dielectric properties of the comet's surface, Kamoun et al. (2014) uses Arecibo *S*-band radar observations of 67P/CG to infer the average ε_r' for the top metres of the nucleus under the assumption that the observed backscatter is dominated by specular reflections in the optical regime. In other words, despite substantial surface roughness, each small element of the surface can be treated as a facet that primarily yields specular reflections. This approach allows the derivation of surface roughness (average tilt of the facets) and the dielectric constant, but the subsequent estimation of porosity from ε_r' assumes a large penetration depth (~2.5 m) which is difficult to reconcile with the backscattering model as pointed out by the authors (Kamoun et al. 2014). Kamoun et al. (2014) ultimately find that the average dielectric constant of the surface is $\varepsilon_r' = 1.9$–2.1 at *S*-band frequency (2.38 GHz). We now know that the bulk shape of the nucleus is very irregular, and that the surface of the nucleus is relatively hard with ~70 per cent of the surface consisting of exposed consolidated material. Hence, Kamoun et al. (2014)'s result will be treated as a rough estimate of the average dielectric properties of the comet surface.

The SESAME-PP experiment aboard the Philae lander provides a localized measurement of the dielectric properties (in the Hz-kHz range) of the shallow subsurface for comparison with Kamoun et al.'s (2014) results (at 2.4 GHz). Lethuillier et al. (2016) used the permittivity probe aboard Rosetta to measure ε_r' in the upper metre of consolidated material at Philae's final landing site Agilkia on 67P/CG, which is the location corresponding to images (d)–(f) in Fig. 2, and which is in shadow throughout most of the nucleus' rotations – suggesting that this site is most likely below the average surface temperature of 200 K. From these measurements, Lethuillier et al. (2016) determined that $\varepsilon_{r\ consol}' \geq 2.45 \pm 0.20$ for the frequency range of ~10 Hz–10 kHz. As previously explained, $\varepsilon_{r\ SESAME\text{-}PP}'$ will be treated as an upper limit for the measurement of $\varepsilon_{r\ consol}'$.

At 90 MHz, the average dielectric properties of comet nucleus interior, i.e. $\gtrsim$10 m depth, have been directly measured using the propagation time-delay of CONSERT's transmitted radiowaves through the comet's head (Kofman et al. 2015). The average ε_r' is inferred to be 1.27 ± 0.05, and is treated as a uniform value at multimetre scales following the subsurface Hypothesis A introduced in Fig. 1(c). Additionally, Ciarletti et al. (2015) use first-order 2D ray-tracing methods to estimate the dielectric constant of the comet head, and find that ε_r' may decrease through the interior (over a thickness of potentially 10–400 m) along the radar signal's path between Philae and the Rosetta orbiter. This result could be attributed to the expected porosity gradient between the sintered consolidated layer and the deeper, porous inner comet head below at least 10 m depth.

In the following section, we employ the geophysical model of a homogeneous interior (Hypothesis A) that consists of a porous dust–ice mixture with homogeneous dielectric properties. We address the alternative Hypothesis B of a heterogeneous interior in Section 5. Table 1 summarizes the geophysical constraints for the three primary layers of Comet 67P/CG's nucleus, as well as the above constraints on their dielectric properties.

4 POST-RENDEZVOUS DIELECTRIC MODELLING OF COMET 67P/CG'S NUCLEUS FOR A HOMOGENEOUS INTERIOR

In the previous sections, we re-characterized the textural, structural, geophysical, and dielectric properties of Comet 67P/CG's nucleus using post-rendezvous knowledge gained from the Rosetta mission, which thereby challenge some of the underlying assumptions that were used to generate our pre-rendezvous dielectric

Table 1. Geophysical and dielectric constraints for the primary layers of Comet 67P/CG's nucleus.

Layer	Thickness h	Porosity P	Dust-to-ice mass ratio $M_{d/i}$	Real Permittivity ε_r'	Texture/Structure
Thick fine-grained dust-ice deposits[a]	1–2 m[a]	~85%[b,c]	(4 ± 2)[d,e,f]	≤1.9–2.1 [g] (averaged over the surface at 8.4 GHz)	~30 % surface coverage; Smooth at metre to decametre scales[h]
Consolidated dust-ice material[a]	≥1–5 m[b], (0–50 cm dust cover)[i]	< 50 %[j] 30–65 %[k]	≥3[l]	≤1.9–2.1 [g] (averaged over the surface at 8.4 GHz) > 2.45 ± 0.20[j] (at 10–10^4 Hz)	~70 % surface coverage; Rocky/rough, consolidated[h]
Primordial dust-ice interior	*(remaining subsurface)*	75–85 %[m]	≥3[l]	1.27 ± 0.05 [m] (at 90 MHz)	Homogeneous on the scale of tens of metres[m]

Notes.[a]El-Maarry et al. (2015a); [b] Kossacki et al. (2015); [c] Fornasier et al. (2016); [d]Rotundi et al. (2015); [e]Thomas et al. (2015); [f] Fulle et al. (2017); [g] Kamoun et al. (2014); [h] Birch et al. (2017); [i] Mottola et al. (2015); [j] Lethuillier et al. (2016); [k] Spohn et al. (2015); [l] Fulle et al. (2019); [m] Kofman et al. (2015)

Table 2. Dielectric properties of the surface and shallow subsurface within the valid range of $\varepsilon_r'_{(s)dust}$ as a function of dust-to-ice mass ratio and the solid density of cometary dust, corresponding to the results of Fig. 3.

				Constrained range of dielectric properties		
Dust-to-ice mass ratio $M_{d/i}$	Dust mass fraction ϕ_{dust}	Solid density of cometary dust $\rho_{(s)dust}$ (kg m^{-3})	Volumetric dust fraction of bulk nucleus interior $f_{dust\ (interior)}$	Cometary dust (at $P = 0$ %) $\varepsilon_r'_{(s)dust}$	Thick fine-grained deposits ($P = 55$–70 %) $\varepsilon_r'_{depos}$	Consolidated material ($P = 30$–65 %) $\varepsilon_r'_{consol}$
3 (2)[a]	75 % (67 %)[a]	2000	20 %	≤2.1	≤1.6	≤2.0
		2800	14 %	≤2.9	≤1.7	≤2.3
		3500	11 %	≤3.8	≤1.8	≤2.6
5 (4)	83 % (80 %)	2000	22 %	≤2.4	≤1.6	≤2.0
		2800	16 %	≤3.3	≤1.7	≤2.5
		3500	13 %	≤4.6	≤1.8	≤2.9
7 (6)	88 % (86 %)	2000	23 %	≤2.5	≤1.6	≤2.1
		2800	16 %	≤3.5	≤1.8	≤2.6
		3500	13 %	≤5.0	≤1.9	≤3.2

Note.[a] Table items in parentheses '()' specifically characterize thick, fine-grained deposits on the nucleus surface

models of 67P/CG (Heggy et al. 2012). Herein, we present the updated, post-rendezvous dielectric model of 67P/CG's nucleus using the structural model developed in Section 2, and the constrained ranges of $\varepsilon_r'_{(s)dust}$, $\varepsilon_r'_{(s)ice}$, $\rho_{(s)dust}$, $\rho_{(s)ice}$, P, and $M_{d/i}$ described in Section 3 for the three primary layers of the nucleus (i.e. fine-grained deposits, consolidated material, and the bulk interior).

4.1 Approximating the effective dielectric constant of cometary dust–ice mixtures

To calculate the effective complex dielectric constant ε_{eff} of a multiphase mixture with different volume fractions f of dust, ice, and vacuum (porosity), we employ the Maxwell Garnett dielectric mixing formula (Sihvola 1999):

$$\varepsilon_{eff} = \varepsilon_e + 3\varepsilon_e \frac{\sum_i f_i \left(\frac{\varepsilon_i - \varepsilon_e}{\varepsilon_i + 2\varepsilon_e}\right)}{1 - \sum_i f_i \left(\frac{\varepsilon_i - \varepsilon_e}{\varepsilon_i + 2\varepsilon_e}\right)}, \quad (1)$$

where ε_e is the complex relative dielectric constant of the host material; ε_i is the complex relative dielectric constant of inclusion phase i of the mixture; and f_i is the volume fraction of inclusion phase i. Cometary dust and ice are modelled as having zero micro or macro porosity. When the bulk porosity of a given layer is $\gtrsim$50 per cent, vacuum is considered the host medium. When calculating the effective dielectric constant of the consolidated layer at a bulk porosity of 30 per cent, cometary dust (with zero porosity) acts as the host material while cometary ice and vacuum (porosity) are inclusions.

The Maxwell Garnett formula assumes that discrete, spherical inclusions are isolated from each other, embedded in a matrix, and are at least 10 times smaller than the radar wavelength – i.e. in the case of X-band radar frequency, $d_{incl} \lesssim 0.4$ cm; for S-band radar, $d_{incl} \lesssim 1.5$ cm; and for VHF radar such as CONSERT, $d_{incl} \lesssim 30$ cm.

To invert CONSERT's measurements of $\varepsilon_r'_{interior}$ to assess the dielectric properties of the porous dust and ice components of Comet 67P/CG, Kofman et al. (2015) and Hérique et al. (2016) use Hashin-Shtrikman bounds of the effective dielectric constant (Sihvola 1999) to calculate the full range of theoretically possible ε_{eff} values for a given mixture. The Maxwell Garnett formula is shown to correspond to the lower Hashin-Shtrikman bound (Sihvola 1999; Hérique et al. 2016) which represents to the lower theoretical limit of ε_{eff} for the different porous mixtures of dust and ice on 67P/CG. Hérique et al. (2016) show that the upper Hashin-Shtrikman bound provides underestimated values of the dielectric constant of cometary dust at zero porosity (i.e. $\varepsilon_r'_{(s)dust}$) and that this limit does not introduce additional constraints of interest on dust materials in the case of 67P/CG, as the aim of Hérique et al. (2016)'s study is to find dust analogue candidates with very low dielectric constants.

Our dielectric model is therefore constructed using the Maxwell Garnett equation to assess the upper limit of $\varepsilon_r'_{(s)dust}$ and thereby constrain our estimates of $\varepsilon_r'_{eff}$ of thick fine-grained dust-ice deposits, and of the consolidated material layer. Since volume

fractions $f_{\rm dust}$ and $f_{\rm ice}$ are not directly constrained by Rosetta's observations of 67P/CG, equation (1) can be rewritten as a function of porosity P, dust-to-ice mass ratio $M_{\rm d/i}$ and solid densities $\rho_{\rm (s)dust}$ and $\rho_{\rm (s)ice}$ using the following relationships:

$$f_{\rm dust} = (1 - P)\left[1 + \frac{\rho_{\rm (s)dust}}{\rho_{\rm (s)ice} M_{\rm d/i}}\right]^{-1}, \quad (2)$$

$$f_{\rm ice} = 1 - P - f_{\rm dust} \quad (3)$$

where for the interior of the comet, we consider the additional constraint that its bulk density $\rho_{\rm bulk}$ has been measured:

$$\rho_{\rm bulk} = f_{\rm dust}\rho_{\rm (s)dust} + f_{\rm ice}\rho_{\rm (s)ice} \quad (4)$$

such that:

$$P_{\rm interior} = 1 - \rho_{\rm bulk}\left(\frac{1 + M_{\rm d/i}}{\rho_{\rm (s)dust} M_{\rm d/i} + \rho_{\rm (s)ice}}\right). \quad (5)$$

Additionally, $M_{\rm d/i}$ can also be converted to dust mass fraction $\phi_{\rm dust}$, which is more commonly used in dielectric modelling (e.g. Heggy et al. 2012):

$$\phi_{\rm dust} = M_{\rm d/i}\left(1 + M_{\rm d/i}\right)^{-1}. \quad (6)$$

In Fig. 3, we generate several plots of ${\varepsilon_{\rm r}}'_{\rm eff}$ at different P as a function of ${\varepsilon_{\rm r}}'_{\rm (s)dust}$ and summarize the results in Table 2. The top row has been calculated for $M_{\rm d/i} = 3$ ($M_{\rm d/i\ (depos)} = 2$); in the middle row, $M_{\rm d/i} = 5$ ($M_{\rm d/i\ (depos)} = 4$); and along the bottom row, $M_{\rm d/i} = 7$ ($M_{\rm d/i\ (depos)} = 6$). The first column of plots has $\rho_{\rm (s)dust} = 2000\,{\rm kg\,m^{-3}}$, the middle column has $\rho_{\rm (s)dust} = 2800\,{\rm kg\,m^{-3}}$, and the third column has $\rho_{\rm (s)dust} = 3500\,{\rm kg\,m^{-3}}$.

For the interior of the comet, we first use equation (5) to calculate the minimum and maximum $P_{\rm interior}$ that satisfy $\rho_{\rm bulk}$ at $\rho_{\rm (s)ice} = 931\,{\rm kg\ m^{-3}}$ (the lower density limit for H_2O: CO_2: CO = 94:3:3 per cent as defined in Section 3.2) and $1138\,{\rm kg\,m^{-3}}$ (the upper density limit for H_2O: CO_2: CO = 75:8:17 per cent, also defined in Section 3.2) (Hérique et al. 2016). The volumetric fractions $f_{\rm dust}$ and $f_{\rm ice}$ are then calculated from equations (2) and (3), and input in equation (1) to calculate ${\varepsilon_{\rm r}}'_{\rm interior}$.

The resulting formulae for the upper few-hundred metres of the nucleus interior are plotted in Fig. 3 as functions of ${\varepsilon_{\rm r}}'_{\rm (s)dust}$ from 1.5 to 5.4 (black curves), and the transparent area in each plot indicates the range of ${\varepsilon_{\rm r}}'_{\rm (s)dust}$ values for which ${\varepsilon_{\rm r}}'_{\rm interior}$ satisfies ${\varepsilon_{\rm r}}'_{\rm CONSERT} = 1.27 \pm 0.05$. Values of ${\varepsilon_{\rm r}}'_{\rm (s)dust}$ incompatible with ${\varepsilon_{\rm r}}'_{\rm CONSERT}$ are whited out. We repeat calculations of ${\varepsilon_{\rm r}}'_{\rm eff}$ for thick fine-grained dust-ice deposits at $P = 55$ per cent and 70 per cent (blue curves) and for consolidated material at $P = 30$ per cent, 50 per cent, and 65 per cent (red curves). Observational constraints on the dielectric properties of the primary layers of 67P/CG are then indicated by horizontal lines in Fig. 3 for: (a) the consolidated surface material as constrained by SESAME-PP (Lethuillier et al. 2016); (b) the average ${\varepsilon_{\rm r}}'$ of the surface as constrained by Arecibo (Kamoun et al. 2014); and (c) the average ${\varepsilon_{\rm r}}'$ of the interior of the nucleus head as constrained by CONSERT (Kofman et al. 2015).

4.2 Dielectric properties of fine-grained deposits, consolidated material, and the homogeneous pristine interior

The resulting 3D dielectric model of 67P/CG is shown in Fig. 4 for the surface and bulk subsurface (employing the hypothesis of a homogeneous interior). Overall, higher values of ${\varepsilon_{\rm r}}'$ are associated with lower porosities, higher dust content, and a higher solid density of cometary dust. Thick fine-grained deposits on the surface are shown to have ${\varepsilon_{\rm r}}'_{\rm depos} > {\varepsilon_{\rm r}}'_{\rm interior}$ where ${\varepsilon_{\rm r}}'_{\rm depos} \leq 1.6$–$1.9$ (light purple surface terrain in Figs 4a–c). Within the constrained parameter space defined in Sections 2 and 3, ${\varepsilon_{\rm r}}'_{\rm depos}$ appears only weakly dependent on the ratio of dust-to-ice, the solid density of constituent dust grains, or our estimate of solid permittivity of cometary dust. This suggests that the relatively high porosity of thick fine-grained dust-ice deposits ($P \gtrsim 55$ per cent) dominates the dielectric properties of this type of terrain.

Consolidated material (exposed over ∼70 per cent of the surface and continuous to at least 5 m depth) has ${\varepsilon_{\rm r}}'_{\rm consol} \approx 2.0$–$3.2$ and corresponds to the dark blue surface terrain shown in Figs 4(a)–(c). Because fine-grained deposits have a lower dust-to-ice mass ratio than the consolidated material, and a higher porosity by ∼10–20 per cent (since the deposits are re-deposited fragments of the consolidated material layer), we find that ${\varepsilon_{\rm r}}'_{\rm depos}$ is 20–40 per cent lower than ${\varepsilon_{\rm r}}'_{\rm consol}$. This model of ${\varepsilon_{\rm r}}'_{\rm consol}$ is consistent with SESAME-PP's shallow subsurface measurement of ${\varepsilon_{\rm r}}'_{\rm consol} \approx 2.45 \pm 0.20$ at the kHz range, which ultimately serves as an upper limit for Earth-based and CONSERT radar observations in the non-dispersive MHz-to-GHz range (as explained in Section 3.5). Kamoun et al.'s (2014) analysis of Arecibo radar observations of 67P/CG yield an average surface dielectric constant of ${\varepsilon_{\rm r}}'_{\rm surf} \approx 1.9$–$2.1$ and is compatible with our model of a surface that is dominated by consolidated material of a higher dielectric constant that is interspersed with thick deposits of fine-grained material with a much lower dielectric constant. The case of a homogeneous interior (Hypothesis A; Fig. 1c) is shown in purple in Fig. 4(d) with a uniform distribution of dust, ice, and porosity and is represented by a single value of ${\varepsilon_{\rm r}}'_{\rm interior} = 1.27 \pm 0.05$ (Kofman et al. 2015).

Constrained by $\rho_{\rm bulk} = 533 \pm 6\,{\rm kg\,m^{-3}}$ (Pätzold et al. 2016), $M_{\rm d/i} = 3$–7 (Fulle et al. 2017; Fulle et al. 2019; Pätzold et al. 2019), $\rho_{\rm (s)ice} = 931$–$1138\ {\rm kg\ m^{-3}}$ (from Section 3.2), and ${\varepsilon_{\rm r}}'_{\rm (s)ice} = 2.7$–$3.3$ (from Section 3.5), we also find that the largest possible value of ${\varepsilon_{\rm r}}'_{\rm (s)dust}$ is 5.02, which is shown by the transparent area in the bottom rightmost plot of Fig. 3. However, this maximum ${\varepsilon_{\rm r}}'_{\rm (s)dust}$ assumes a maximum $M_{\rm d/i} = 7$. Since Fulle et al. (2017, 2019) have only established that $M_{\rm d/i} > 3$, we have computed the maximum ${\varepsilon_{\rm r}}'_{\rm (s)dust}$ for higher values of $M_{\rm d/i}$ and find a best-fitting formula of ${\rm Max}\{{\varepsilon_{\rm r}}'_{\rm (s)dust}\} = -5.6\ M_{\rm d/i}^{(-0.71)} + 6.45$, which is valid over the range of $M_{\rm d/i} = 3$–300.

Finally, we compare our results with the plot shown in Hérique et al. (2016)'s Fig. 6 to validate our model. If $M_{\rm d/i} = 6$, $\rho_{\rm (s)ice} = 1171\,{\rm kg\,m^{-3}}$ and ${\varepsilon_{\rm r}}'_{\rm (s)ice} = 3.0$, we find the same maximum ${\varepsilon_{\rm r}}'_{\rm (s)dust}$ and corresponding $f_{\rm dust}$ of the bulk nucleus interior at a given value of $\rho_{\rm (s)dust}$. For example, at $\rho_{\rm (s)dust} = 3500\,{\rm kg\,m^{-3}}$, fig. 6 by Hérique et al. (2016) yields ${\varepsilon_{\rm r}}'_{\rm (s)dust} \approx 4.65$ and $f_{\rm dust} \approx 13$ per cent. Our model yields consistent results: a maximum of ${\varepsilon_{\rm r}}'_{\rm (s)dust} = 4.63$ with $f_{\rm dust} = 12.9$ per cent at $M_{\rm d/i} = 6$.

5 UPPER LIMIT ON THE SIZE OF PRIMORDIAL COMETARY BUILDING BLOCKS

Having established the 3D dielectric model of 67P/CG for the case of a homogeneous nucleus interior, we now explore the possible occurrence of metre-sized to multimetre-sized blocks in the subsurface (which may represent the primordial building blocks of the cometary nucleus) and set upper limits on their size and dielectric contrast.

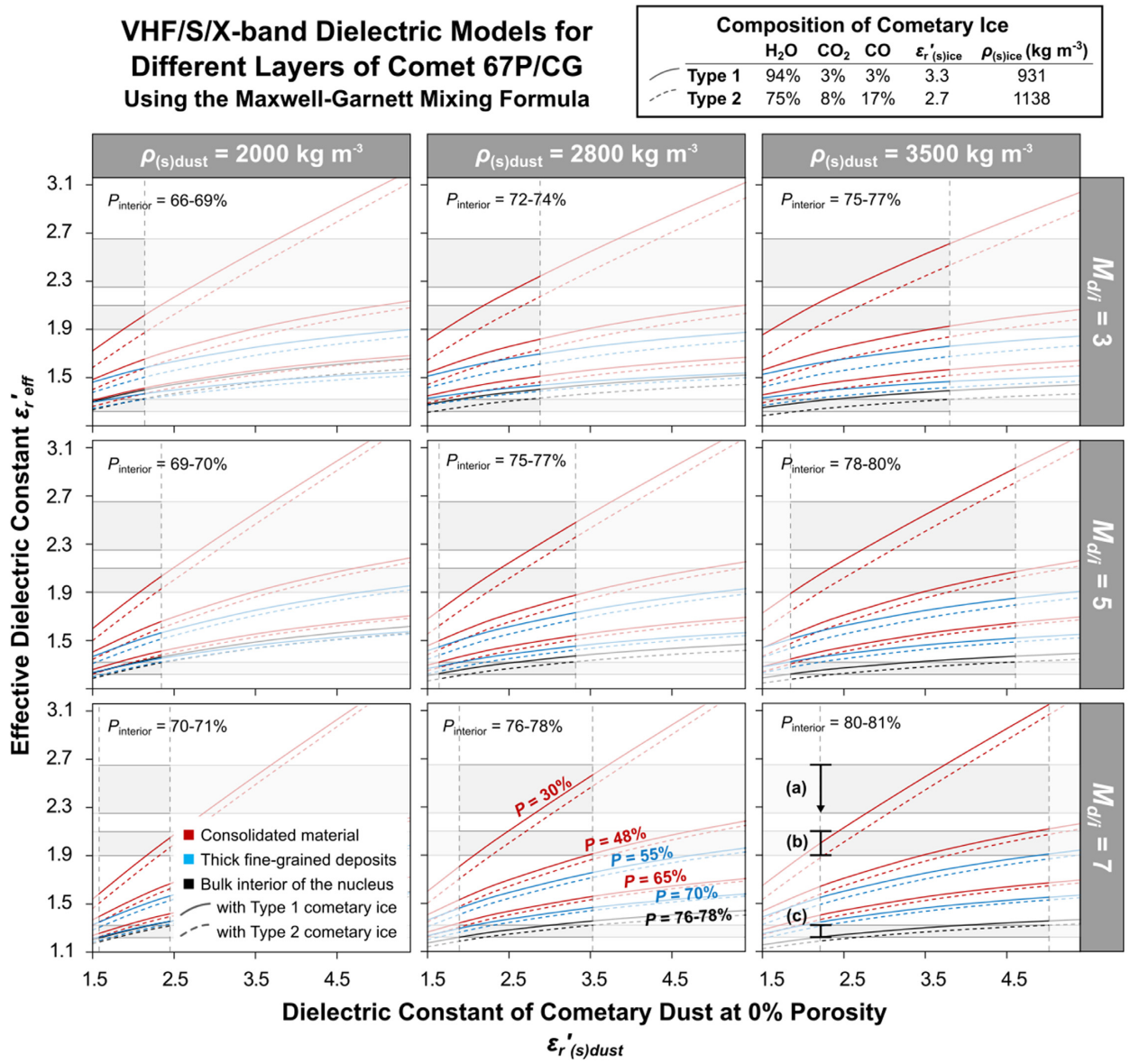

Figure 3. The effective dielectric constant $\varepsilon_r{}'_{\rm eff}$ of the three primary layers of Comet 67P/CG's nucleus as a function of solid dust permittivity $\varepsilon_r{}'_{\rm (s)dust}$, the layer's bulk porosity P, its dust-to-ice mass ratio $M_{\rm d/i}$, and the solid densities of cometary dust $\rho_{\rm (s)dust}$ and ice $\rho_{\rm (s)ice}$. Plots are arranged by increasing $M_{\rm d/i}$ from top to bottom, and increasing $\rho_{\rm (s)dust}$ from left to right. The bottom middle plot, for example, shows $\varepsilon_r{}'_{\rm eff}$ of each layer as a function of $\varepsilon_r{}'_{\rm (s)dust}$ at $\rho_{\rm (s)dust} = 2800\,{\rm kg\,m^{-3}}$ and $M_{\rm d/i} = 7$ ($M_{\rm d/i\,(depos)} = 6$). The dielectric constant of thick fine-grained deposits $\varepsilon_r{}'_{\rm depos}$ are plotted in blue for $P = 55$–70 per cent; consolidated material $\varepsilon_r{}'_{\rm consol}$ in red for $P = 30$–65 per cent; and the nucleus interior $\varepsilon_r{}'_{\rm interior}$ in black for $P = 76$–78 per cent (which is calculated from equation 5 given that $\rho_{\rm bulk} = 533 \pm 6\,{\rm kg\,m^{-3}}$). Here, the intersection of $\varepsilon_r{}'_{\rm CONSERT}$ with $\varepsilon_r{}'_{\rm interior}$ constrains $\varepsilon_r{}'_{\rm (s)dust} = 1.9$–$3.5$ (the transparent area). Observational constraints on $\varepsilon_r{}'$ by SESAME-PP, Arecibo, and CONSERT are indicated by horizontal grey lines, as denoted by brackets (a), (b), and (c), respectively, in the bottom right plot.

When radar waves encounter dielectric heterogeneities within a host material (with dimensions proportional to the wavelength, such as dense boulders buried in loose dust), this generates volume scattering that is observed as dispersion or broadening of the received signal (in the time-domain) with respect to the width of the initially transmitted radar pulse (e.g. Kofman et al. 1998; Carley & Heggy 2008; Kofman et al. 2015; Ciarletti et al. 2017). While CONSERT has observed slightly broader pulses from 67P/CG relative to the reference values determined from ground calibration measurements, the received signals do not exhibit other characteristics of volume scattering, such as increased pulse broadening in association with longer distances travelled through the nucleus, or asymmetry in the pulse shape (Ciarletti et al. 2017). As a result, any heterogeneous blocks in the nucleus interior must be (1) sufficiently

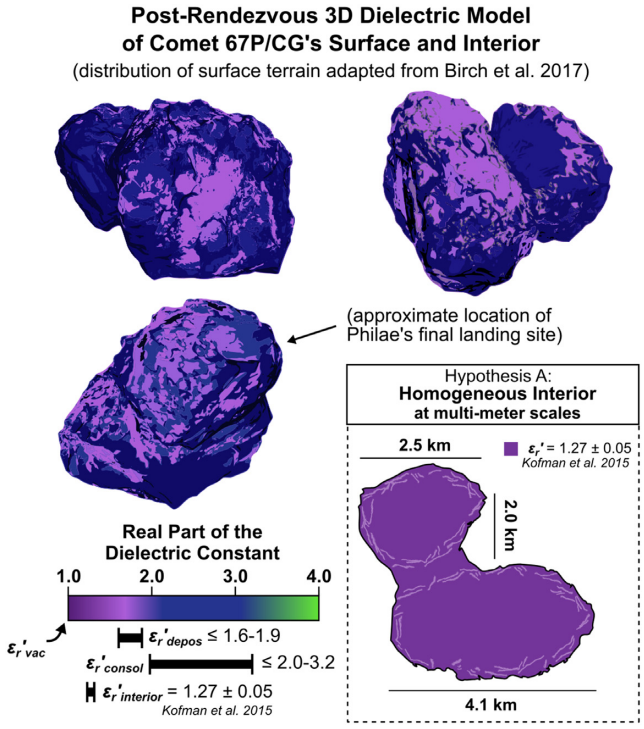

Figure 4. 3D dielectric model of the surface and interior of Comet 67P/CG at different perspectives. The surface is dielectrically heterogeneous at large spatial scales unlike asteroid regoliths. About 30 per cent of the surface has $\varepsilon_r' \leq 1.6$–1.9 due to thick deposits of loose fine-grained blocks <1 m in diameter, while 70 per cent of the surface has a higher $\varepsilon_r' \leq 2.0$–3.2. The dielectric properties of the interior of the head was measured by CONSERT aboard Rosetta and ε_r' is just as low as fine-grained deposits (Kofman et al. 2015). Hypothesis A of a dielectrically homogeneous interior is shown for the deep subsurface assuming that both nucleus lobes have separate stratification in the upper few hundred metres (Massironi et al. 2015), but that each lobe can be treated as having similar formation histories and therefore similar compositions and dielectric properties.

small in scale below CONSERT's transmitted radar wavelength; (2) much larger than CONSERT's radar wavelength (where $\lambda \approx 3$ m in vacuum); and/or have (3) weak dielectric contrast ($\Delta\varepsilon_r'$) with respect to the measured average of $\varepsilon_{r\,\mathrm{interior}}' = 1.27 \pm 0.05$ (Kofman et al. 2015), which would suggest that any multimetre-sized blocks have a similar porosity P and dust-to-ice ratio $M_{d/i}$ as the surrounding matrix.

Ciarletti et al. (2017) set upper limits on the possible dielectric contrast of 1–10 m-sized subsurface scatterers by simulating radar-wave propagations through the nucleus interior for three different sizes of blocks in the subsurface (diameters of 1, 3, and 8 m) and by varying the dielectric contrast $\Delta\varepsilon_r' = \varepsilon_{r\,\mathrm{max}}' - \varepsilon_{r\,\mathrm{min}}'$ of the blocks with respect to the surrounding matrix. Ciarletti et al. (2017) measure the resulting signal broadening of the propagated radar wave, and match this with CONSERT's observed signal widths to determine the limits of $\Delta\varepsilon_r'$ for a given size of subsurface block. Ciarletti et al. (2017) find that blocks $\lesssim$1 m in diameter will not cause measurable signal broadening for any $\Delta\varepsilon_r'$, while blocks the size of the radar wavelength or larger (i.e. $\gtrsim$3 m) must have $|\Delta\varepsilon_r'| \lesssim 0.25$ to be compatible with CONSERT's lack of observed signal broadening. However, we note that Ciarletti et al. (2017) conduct their propagation studies at discrete values of $\Delta\varepsilon_r'$ at intervals of about 0.10 (see Ciarletti et al. 2017's fig. 10), suggesting that the upper limit of $|\Delta\varepsilon_r'|$ may actually be between 0.15 and 0.25 for spheres >1 m. Hence, we define subsurface blocks that have $|\Delta\varepsilon_r'| \gtrsim 0.25$ as having 'strong' dielectric contrast, $0.15 \lesssim |\Delta\varepsilon_r'| \lesssim 0.25$ as having 'moderate' dielectric contrast, and $|\Delta\varepsilon_r'| \lesssim 0.15$ as having 'weak' dielectric contrast with the surrounding matrix. Hence, if blocks in the subsurface have strong $|\Delta\varepsilon_r'|$, then they must also be $\leq$1 m in diameter; if the blocks have moderate $|\Delta\varepsilon_r'|$, then they are likely $\leq$1 m in diameter; or if the blocks have weak $|\Delta\varepsilon_r'|$, then there is no particular limit on their size.

As first described in Section 2.3, ~3 m-sized surface bumps on 67P/CG have been observed on the walls of deep cavities (which reach a few hundred metres in depth) and are postulated to be the primordial building blocks of the comet interior (Sierks et al. 2015; Davidsson et al. 2016). If surface bumps are primordial in nature, then they should be continuous throughout the subsurface – yet given their size, must also have sufficiently weak dielectric contrast $|\Delta\varepsilon_r'|$ to introduce no measurable volume scattering in CONSERT's observations of the comet interior.

We investigate the possibility that surface bumps are continuous in the subsurface by estimating their dielectric contrast $\Delta\varepsilon_r'$ with respect to the subsurface matrix material in which they are embedded. We follow a similar approach as that of Nunes and Phillips (2006), who estimate $\Delta\varepsilon_r'$ between adjacent martian polar layered deposits of water–ice/dust mixtures that have different optical albedos and therefore different volumetric fractions of dust. To estimate $\Delta\varepsilon_r'$ from differences in albedo on the surface of 67P/CG, we employ the same relationship that Nunes and Phillips (2006) utilized to estimate dust mass fraction from albedo, adapted to Comet 67P/CG – specifically, that of Kieffer (1990).

Our approach is then divided into three steps: (1) determine the albedo contrast ΔA of 67P/CG's ~3 m-sized surface bumps relative to their surrounding matrix material using OSIRIS imagery; (2) estimate the volumetric dust fraction of 67P/CG's surface bumps $f_{\mathrm{dust(bumps)}}$ and of the surrounding matrix $f_{\mathrm{dust(mtrx)}}$ using Kieffer's (1990) semi-empirical model relating albedo A and dust mass fraction ϕ_{dust}; and lastly (3) calculate $\Delta\varepsilon_{r\,\mathrm{eff}}'$ between the surface bumps and their surrounding terrain by inputting each f_{dust} into the Maxwell Garnett dielectric mixing law and calculating the difference.

5.1 Albedo contrast in the subsurface as observed by OSIRIS

The following image acquired by the OSIRIS narrow-angle camera (NAC) shows the walls of the Seth 01 pit on the body of 67P/CG (Figs 5a–c) and provides a clear example of the bumpy surface texture that is hypothesized to represent a heterogeneous distribution of dust and ice in the upper hundreds of metres of the subsurface (Sierks et al. 2015; Davidsson et al. 2016). Since albedo variation appears subtle between bumps in Fig. 5, we cannot exclude the possibility that initial exposures of subsurface ice have sublimated away, yielding a homogeneous dust cover that obscures albedo contrast in the subsurface. Instead, we propose that the neighbouring Aswan cliff, located within ~100 m from Seth 01, bears the same characteristic bumpy surface texture (comparing Figs 5a–c with Figs 5d–f) and that the partial collapse of the Aswan cliffside partway through the Rosetta mission, observed both before and after by OSIRIS, has exposed fresh underlying material that would be ideal for investigating albedo contrast in the immediate subsurface beneath the bumpy surface texture (Pajola et al. 2017).

Pajola et al. (2017) compute the normal albedo of the freshly exposed cliffside material of Aswan in six different regions of interest (ROIs) at 11 different wavelengths in the visible frequency range that correspond to different OSIRIS NAC filters. In line with

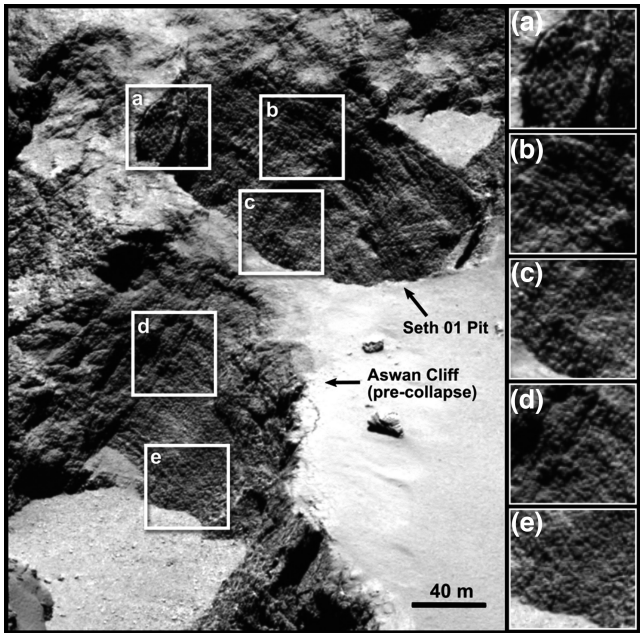

Figure 5. High-resolution image acquired on 2015 March 20 by the OSIRIS NAC showing the bumpy surface texture on the wall of a deep pit on Comet 67P/CG, as well as the face of a neighbouring cliffside. Comparison of subpanels (a)–(e) shows that the bumpy texture of the Seth 01 pit walls at a few metres' scale appears very similar to that of the Aswan cliffside. If the same geologic processes can explain the surface texture of both features, then we are able to use studies of the Aswan cliff collapse (which exposed fresh ice in the comet subsurface) to assess potential heterogeneity in the distribution of the dust-to-ice ratio at the scale of a few metres.

Nunes and Phillips' (2006) analysis that uses 650 nm images to assess albedo, we use Pajola et al.'s (2017) albedo values that have been computed at the 649.1 nm-centred filter of OSIRIS NAC images.

Two of the six ROIs are located outside the collapsed region on the unaltered cliff top (see Pajola et al. 2017's fig. 3g) and exhibit the same normal albedo as the average nucleus surface, $A_{\rm surf} \approx 0.065$ (Fornasier et al. 2015; Pajola et al. 2017). Among the three ROIs that encompass bright, freshly exposed material, Pajola et al. (2017) measure normal albedos that range from $A = 0.15$ to $A \gtrsim 0.41$ at 649.1 nm. We treat the darker ROI as the subsurface matrix, and the brightest ROI as potential primordial blocks (i.e. $A_{\rm mtrx} = 15$ per cent and $A_{\rm blocks} \gtrsim 41$ per cent).

5.2 Estimation of relative dust mass fraction from albedo contrast

In order to infer differences in dust mass fraction for normal albedos A of 0.15 and 0.41 on 67P/CG (Pajola et al. 2017), we employ the semi-empirical model by Kieffer (1990) that relates 'apparent' albedo $A_{\rm app}$ to dust mass fraction $\phi_{\rm dust}$ for different dust and ice grain sizes, and adapt it to the subsurface of Comet 67P/CG under the following assumptions.

5.2.1. The dependence of apparent and normal albedo on dust mass fraction

Kieffer's (1990) model is tailored to the northern polar layered deposits of Mars, where 'apparent' albedo $A_{\rm app}$ is the brightness of an isotropically scattering surface when illuminated at a solar incidence angle of $i = 70^\circ$, relative to that of a perfectly reflecting isotropically scattering surface illuminated at $i = 0^\circ$ (Hapke, 1981). In this context, 'apparent' albedo is synonymous with the 'radiance factor' (*I/F* or RADF) of an isotropically scattering surface illuminated at $i = 70^\circ$ (Hapke, 2012). fig. 7 of Kieffer (1990) shows the decrease of $\mathrm{RADF}_{i=70^\circ}$ as a function of increasing $\phi_{\rm dust}$, as well as with increasing dust and ice grain diameters $d_{\rm dust}$ and $d_{\rm ice}$, respectively. Subsequently, Appendix Figs A1 and A2, adapted from Kieffer (1990), show that as the ratio $d_{\rm dust}/d_{\rm ice}$ decreases, smaller amounts of $\phi_{\rm dust}$ are needed to reduce $\mathrm{RADF}_{i=70^\circ}$ to the same minimum $\mathrm{RADF}_{i=70^\circ}$ of a pure dust deposit. For example, when $d_{\rm dust}/d_{\rm ice} = 0.5$, $A_{\rm app} = A_{\rm min}$ at $\phi_{\rm dust} \gtrsim 50$ per cent, whereas for $d_{\rm dust}/d_{\rm ice} = 0.1$, $A_{\rm app} = A_{\rm min}$ with $\phi_{\rm dust} \gtrsim 1$ per cent.

For Comet 67P/CG, Pajola et al. (2017) measure surface radiance from OSIRIS images of the Aswan cliffside (which were acquired at high phase angles of $\alpha \approx 89^\circ$), and apply a photometric correction factor (defined by Fornasier et al. 2015) to calculate 'normal' albedo A, the brightness that would be observed at $\alpha = 0^\circ$ and $i = 0^\circ$ relative to a perfect Lambertian surface also illuminated at $i = 0^\circ$. Normal albedo A is therefore equivalent to $\mathrm{RADF}_{i=0^\circ}$ at $\alpha = 0^\circ$ of a non-isotropically scattering surface, and subsequently accounts for the increase in reflectance associated with 67P/CG's opposition effect at $\alpha = 0^\circ$ (Fornasier et al., 2015).

Notably, the opposition peak of a dust–ice mixture is also observed to decrease as $\phi_{\rm dust}$ and/or $d_{\rm dust}/d_{\rm ice}$ increases (Yoldi et al., 2015). Specifically, Yoldi et al. (2015) measure the reflectance factor (REFF) at $\alpha = 0^\circ$ for $i = 20^\circ$ for different mass fractions of JSC1-AF lunar simulant dust intimately mixed with either fine- or coarse-grained water-ice – where $\mathrm{RADF}_i \equiv \mathrm{REFF}_i \cos(i)$, and $\mathrm{REFF}_{i=20^\circ} \approx \mathrm{REFF}_{i=0^\circ}$, such that $\mathrm{RADF}_{i\approx 0^\circ} \approx 0.94\ \mathrm{REFF}_{i=20^\circ}$. As shown in fig. 3 of Yoldi et al. (2015), $\mathrm{RADF}_{i\approx 0^\circ}$ reaches a minimum value when $\phi_{\rm dust} \gtrsim 25$ per cent for $d_{\rm dust}/d_{\rm ice} \approx 0.3$, while for a larger $d_{\rm dust}/d_{\rm ice} \approx 5$, the minimum $\mathrm{RADF}_{i\approx 0^\circ}$ is reached when $\phi_{\rm dust} \gtrsim 65$ per cent, consistent with the dependence of $A_{\rm app}$ on $\phi_{\rm dust}$ and $d_{\rm dust}/d_{\rm ice}$ in Kieffer's (1990) model. Hence, we are able to use Kieffer's (1990) model of albedo at 70° solar incidence as a reasonable estimate for the dependence of 67P/CG's normal albedo on $\phi_{\rm dust}$.

5.2.2. Dust and ice grain shapes and sizes

Kieffer's (1990) model is based partly on Mie scattering theory, which is valid for spherical particles that are separated by distances much greater than the observing wavelength (649 nm in our case). Warren (1982), however, finds that potential near-field scattering effects associated with closely packed grains in dirty snow are negligible as long as the centre-to-centre distance between individual particles is much greater than the wavelength. Regarding grain shape, Dang, Fu & Warren (2016) point out that the albedo of non-spherical snow grains can be mimicked by spherical particles with smaller radii. We therefore treat values of dust and ice grain diameters used by Kieffer (1990) as 'effective' scattering diameters (e.g. $d_{\rm dust(eff)}$), as we are interested in retrieving relative dust mass fraction rather than the specific optical properties of the constituent dust and ice particles.

5.2.3. Using external mixing to approximate internal mixing of dust within ice

Kieffer (1990) also assumes an external mixture of dust and ice particles as opposed to an internal mixture. For the latter, dust grains

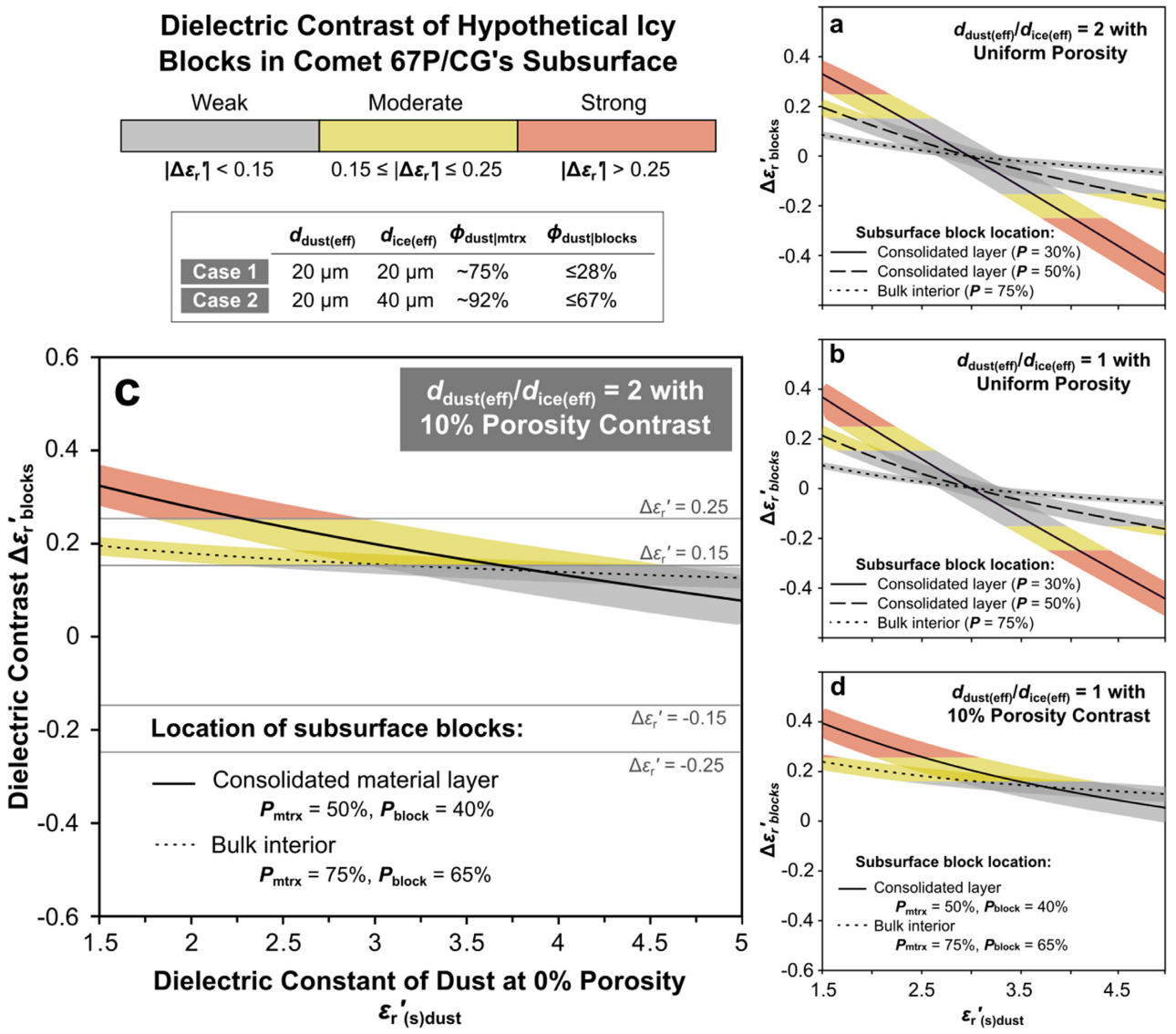

Figure 6. Estimated dielectric contrast of icy blocks within the consolidated material layer or the bulk interior of the nucleus. In plots (b) and (d), dust mass fraction ϕ_{dust} has been calculated from the albedo contrast between the subsurface matrix and heterogeneous blocks when dust and ice grains have the same effective scattering diameter ($d_{dust(eff)}/d_{ice(eff)} = 1$). In plots (a) and (c), ϕ_{dust} has been calculated for $d_{dust(eff)}/d_{ice(eff)} = 2$. In all four panels, $\Delta\varepsilon_r{}'_{blocks}$ is calculated (using equation 6) as a function of $\varepsilon_r{}'_{(s)dust}$ for $\varepsilon_r{}'_{(s)ice} = 2.7$, 3.0, and 3.3 (setting the width of the highlighted range that bounds each curve) for either uniform porosity (a and b) or a more porous matrix relative to the blocks (c and d). Red indicates strong $\Delta\varepsilon_r{}'_{blocks}$, yellow indicates moderate $\Delta\varepsilon_r{}'_{blocks}$, and grey indicates weak $\Delta\varepsilon_r{}'_{blocks}$ that would induce no measurable volume scattering, consistent with observations of the inner comet head by CONSERT. Plots (c) and (d) correspond to the most likely hypothesis – non-uniform porosity between subsurface blocks and the matrix material.

are encapsulated by ice, as is thought to be the case for the sintered, consolidated layer of 67P/CG's shallow subsurface. Internal mixing effectively increases the scattering cross-section of encapsulated dust grains, and hence increases light absorption, resulting in a lower albedo than an external mixture of the same amount of dust and ice (Chýlek, Ramaswamy & Srivastava 1983; Liou et al. 2014). As a result, Kieffer's (1990) model will likely overestimate ϕ_{dust} for Comet 67P/CG at a given albedo. However, we are interested in the relative difference in dust mass fraction between primordial blocks and the surrounding subsurface matrix rather than absolute values of ϕ_{dust}, and whether for internal or external mixtures, albedo maintains its logarithmic dependence on ϕ_{dust} as demonstrated by the radiative transfer modelling of dirty snow albedo at 550 nm by Liou et al. (2014; fig. 7 therein). Kieffer's (1990) external mixture model therefore provides a first-order approximation to an internal mixture.

5.2.4. Estimating 67P/CG's dust mass fraction from apparent albedo

Fig. 7 of Kieffer (1990) shows a plot of the albedo A of dust–ice mixtures as a function of ice grain size (diameter d_{ice} = 2–2000 μm) for three different effective dust grain sizes ($d_{dust(eff)} = 5$, 20, and 200 μm) and for four different dust mass fractions (ϕ_{dust} = 0.1 per cent, 1 per cent, 10 per cent, and 50 per cent). As previously mentioned, apparent albedo A_{app} decreases with increasing ϕ_{dust}, as well as with increasing d_{ice} or d_{dust}.

Since Kieffer (1990) uses the optical properties of martian atmospheric dust, we select the combination of effective dust grain sizes in Kieffer's (1990) model that yield sufficiently low albedo to match that of the comet. We therefore exclude $d_{\mathrm{dust(eff)}} = 5\,\mu\mathrm{m}$ since the minimum achievable albedo ($A_{\mathrm{min}} = 0.26$; the albedo of a pure dust deposit) is too bright for the low geometric albedos observed on 67P/CG ($A \approx 0.065$; Fornasier et al. 2015). From Kieffer's (1990) plot, pure dust deposits with effective dust grain sizes of $d_{\mathrm{dust(eff)}} = 20$ and 200 μm yield A_{min} of 0.065 and 0.025, respectively.

We replot Kieffer's (1990) results in Supplementary Figs A1 and A2 as A versus ϕ_{dust} for five different effective grain size ratios ($d_{\mathrm{dust(eff)}}/d_{\mathrm{ice(eff)}} = 0.1$, 0.2, 0.5, 1, and 2). Since Kieffer (1990) has only determined A in the range of 0.1 per cent $\leq \phi_{\mathrm{dust}} \leq 50$ per cent, we extrapolate to larger dust mass fractions using the boundary condition that $A = A_{\mathrm{min}}$ at $\phi_{\mathrm{dust}} = 100$ per cent. Fig. A1 is plotted for $d_{\mathrm{dust(eff)}} = 20\,\mu\mathrm{m}$ ($A_{\mathrm{min}} = 0.065$), and Fig. A2 is plotted for $d_{\mathrm{dust(eff)}} = 200\,\mu\mathrm{m}$ ($A_{\mathrm{min}} = 0.025$) to show that for increasing effective dust grain diameters $\gtrsim$20 μm, A_{min} approaches 0, and the dependence of A on ϕ_{dust} primarily changes with the ratio of effective grain size between dust and ice $d_{\mathrm{dust(eff)}}/d_{\mathrm{ice(eff)}}$ rather than the specific grain size of dust or ice. By contrast, as effective dust grain size decreases, A_{min} increases, such that a pure deposit of dust with 5 μm effective grain diameters is brighter ($A_{\mathrm{min}} = 0.26$) than a pure deposit of dust with 20 μm effective grain diameters ($A_{\mathrm{min}} = 0.065$). Comet 67P has an average geometric albedo lower than 0.1, so we therefore only consider effective dust grain diameters $\gtrsim$20 μm. Hence, we are able to treat Fig. A1 as representative of the same dependence on dust mass fraction for any $d_{\mathrm{dust}} \gtrsim 20\,\mu\mathrm{m}$.

The X symbols on each curve mark where $A_{\mathrm{mtrx}} = 0.15$ and $A_{\mathrm{blocks}} = 0.41$, which are the albedos observed from the freshly exposed subsurface of 67P/CG identified in Section 5.1. If the hypothesized primordial blocks are continuous throughout the subsurface, then we can assume that the subsurface matrix combined with the primordial blocks have an average dust-to-ice mass ratio equivalent to that of 67P/CG's bulk interior, i.e. $M_{\mathrm{d/i}} > 3$ (Fulle et al. 2017; Fulle et al. 2019). Using equation (6), this corresponds to an average dust mass fraction of $\phi_{\mathrm{dust(avg)}} \gtrsim 75$ per cent, which is marked in Figs A1 and A2 as a shaded vertical region. Therefore, $\phi_{\mathrm{dust(mtrx)}}$ must be $\geq \phi_{\mathrm{dust(avg)}}$ and $\phi_{\mathrm{dust(blocks)}}$ must be $\leq \phi_{\mathrm{dust(avg)}}$. In other words, for a given curve in Figs A1 and A2, at least one of the X's must be inside the vertical shaded region. In Fig. A1, the curves for $d_{\mathrm{dust(eff)}}/d_{\mathrm{ice(eff)}} = 1$ and $d_{\mathrm{dust(eff)}}/d_{\mathrm{ice(eff)}} = 2$ meet this condition. In Fig. A2, only $d_{\mathrm{dust(eff)}}/d_{\mathrm{ice(eff)}} = 2$ meets this condition. All other curves exhibit unrealistically low dust mass fractions.

From these results, we conclude that Kieffer's (1990) model provides plausible estimates of ϕ_{dust} on Comet 67P/CG at a given albedo for $d_{\mathrm{dust(eff)}} \geq 20\,\mu\mathrm{m}$ and $d_{\mathrm{dust(eff)}}/d_{\mathrm{ice(eff)}} \geq 1$. Hereafter, we consider two cases of effective grain size ratios from Fig. A1 – using Kieffer's (1990) results at $d_{\mathrm{dust}} = 20\,\mu\mathrm{m}$ (Fig. A1) – to derive ϕ_{dust} from albedo A: $d_{\mathrm{dust(eff)}}/d_{\mathrm{ice(eff)}} = 1$ and $d_{\mathrm{dust(eff)}}/d_{\mathrm{ice(eff)}} = 2$. Table 3 lists the resulting dust mass fractions associated with the observed values of A_{mtrx} and A_{blocks}, which will be used as input for the next section.

5.3 Estimation of dielectric contrast in the subsurface

We define the dielectric contrast $|\Delta\varepsilon_{\mathrm{r}}'|$ of subsurface blocks as the difference between the effective dielectric constant of the subsurface matrix material and that of the subsurface blocks:

$$\left|\Delta\varepsilon_{\mathrm{r}}'_{\mathrm{blocks}}\right| = \left|\varepsilon_{\mathrm{r}}'_{\mathrm{eff(blocks)}} - \varepsilon_{\mathrm{r}}'_{\mathrm{eff(mtrx)}}\right|, \quad (7)$$

Table 3. Estimated dust mass fractions of dusty subsurface matrix and hypothetical icy blocks for two different combinations of dust and ice effective grain sizes. Adapted from Kieffer (1990).

Effective grain size ratio $d_{\mathrm{dust(eff)}}/d_{\mathrm{ice(eff)}}$	Estimated dust mass fraction ϕ_{dust}	
	Subsurface matrix ($A = 0.15$)	Primordial blocks ($A \geq 0.41$)
1	75 %	≤27 %
2	92 %	≤67 %

where $\varepsilon_{\mathrm{r}}'_{\mathrm{eff}}$ is calculated separately for primordial blocks and for the subsurface matrix using the Maxwell Garnett mixing formula from equation (1). We will compute equation (7) twice: once for hypothetical blocks in the consolidated material layer, which has a low porosity between 30 and 65 per cent (Spohn et al. 2015), and secondly for hypothetical blocks in the deeper subsurface, which has a high porosity of ∼75–85 per cent (Kofman et al. 2015).

To calculate volumetric fraction f_{dust} from mass fraction ϕ_{dust}, we combine equations (2) and (6) to yield:

$$f_{\mathrm{dust}} = (1 - P_{\mathrm{mtrx}}) \left[1 + \frac{\rho_{\mathrm{(s)dust}}\,(1 - \phi_{\mathrm{dust}})}{\rho_{\mathrm{(s)ice}}\phi_{\mathrm{dust}}}\right]^{-1}, \quad (8)$$

where we assume that the subsurface matrix and primordial blocks have the same composition of cometary dust and the same type of ice – in other words, $\rho_{\mathrm{(s)dust}}$ and $\rho_{\mathrm{(s)ice}}$ are the same for matrix and blocks. Moreover, we assume that the grain size of cometary dust and ice do not change between primordial blocks and their surrounding matrix, as the physical processes that have acted to shape dust and ice particles (e.g. sintering) are expected to act uniformly upon adjacent blocks and their surrounding matrix.

Next, we compute dielectric contrast assuming the porosity is the same for the subsurface matrix and primordial blocks, hence depending solely on differences in dust fraction. If, however, the matrix porosity is greater than that of the blocks – e.g. $P_{\mathrm{mtrx}} = 50$ per cent, $P_{\mathrm{blocks}} = 30$ per cent – then $|\Delta\varepsilon_{\mathrm{r}}'_{\mathrm{blocks}}|$ will be larger than if there is uniform porosity, as will be shown in Fig. 6.

Fig. 6 contains four plots showing the potential parametric space for which the dielectric contrast of subsurface blocks would or would not induce volumetric scattering in CONSERT's 90 MHz radar observations if they are comparable in size to the observing wavelength (∼3 m in vacuum). Figs 6(a) and (b) show the estimated dielectric contrast between blocks and the subsurface matrix that differ in dust fraction but have uniform porosity. Figs 6(c) and (d) show the effect upon dielectric contrast if, in addition to having different dust fractions, the porosity also differs between the matrix and blocks. Note that within the bulk interior of the nucleus, if there is no porosity contrast between the matrix and blocks, their dielectric contrast will be weak (grey), i.e. inducing no measurable volume scattering in CONSERT's radar observations.

Figs 6(b) and (d) are calculated for $d_{\mathrm{dust(eff)}}/d_{\mathrm{ice(eff)}} = 1$ (see Table 3), while Figs 6(a) and (c) correspond to $d_{\mathrm{dust(eff)}}/d_{\mathrm{ice(eff)}} = 2$. Using equation (6), each curve has been computed as a function of $\varepsilon_{\mathrm{r}}'_{\mathrm{(s)dust}}$ along the horizontal axis, and the shaded region surrounding each curve corresponds to the full range of possible values of $\Delta\varepsilon_{\mathrm{r}}'_{\mathrm{blocks}}$ achieved by varying $\rho_{\mathrm{(s)dust}}$, $\rho_{\mathrm{(s)ice}}$, and $\varepsilon_{\mathrm{r}}'_{\mathrm{(s)ice}}$ within the ranges defined in Section 3. Strong dielectric contrast, as defined at the beginning of Section 5, is highlighted in red, while moderate dielectric contrast is in yellow, and weak dielectric contrast in grey.

Since ice-enriched blocks likely have a different bulk density from a matrix with more dust, we suggest that Figs 6(c) and (d) represent the most reasonable characterization of porosity and dust mass fraction differences between subsurface blocks and the matrix – whether located in the consolidated material layer or the bulk interior of the nucleus.

For $d_{\mathrm{dust(eff)}}/d_{\mathrm{ice(eff)}} = 1$, we find that $\Delta\varepsilon_{\mathrm{r}}{}'_{\mathrm{blocks}}$ is weak in the consolidated material layer or bulk interior if there is no porosity difference between the matrix and blocks (Fig. 6a); but with porosity contrast on the order of ∼10–15 per cent, $\Delta\varepsilon_{\mathrm{r}}{}'_{\mathrm{blocks}}$ is moderate to strong (i.e. would induce volume scattering; Fig. 6c). Increasing $d_{\mathrm{dust(eff)}}/d_{\mathrm{ice(eff)}}$ to 2 shows that calculated dielectric contrast between the matrix and subsurface blocks is slightly weaker than at $d_{\mathrm{dust(eff)}}/d_{\mathrm{ice(eff)}} = 1$ but would still induce measurable volumetric scattering if the blocks are comparable in size to CONSERT's wavelength. Overall, it is evident that dielectric contrast within the bulk interior is most strongly dependent on the porosity contrast between subsurface blocks and the surrounding matrix.

Our results suggest that because CONSERT did not observe volume scattering from the bulk interior of the nucleus head (Kofman et al. 2015), any subsurface blocks would need to have low porosity contrast with the surrounding matrix of <10 per cent difference, in agreement with the limit of density variability inferred from dielectric modelling by Hérique et al. (2019) for the case of a fixed dust-to-ice ratio in the nucleus head's interior. However, even without porosity contrast, we find that any heterogeneous blocks located in the consolidated material layer would have sufficient differences in dust fraction from the surrounding matrix material to generate moderate to strong dielectric contrast (where $\varepsilon_{\mathrm{r}}{}'_{\mathrm{(s)dust}} \not\approx \varepsilon_{\mathrm{r}}{}'_{\mathrm{(s)ice}}$) that would induce measurable volume scattering within this layer – unless, as Ciarletti et al. (2017) suggest, these blocks are smaller than 1 m and therefore sufficiently small with respect to CONSERT's characteristic observing radar wavelength of 3.3 m (in vacuum) so as to induce no measurable signal broadening.

We therefore set an upper size limit of ∼1 m on any subsurface blocks that could be located in the sintered layer of consolidated material. Hence, given that the characteristic size of surface bumps overlaying the studied site is 2.5 ± 1 m in diameter (Sierks et al. 2015; Davidsson et al. 2016), the observed strong dielectric contrast of the immediate subsurface indicates that these bumps cannot be continuous beneath the surface, and therefore do not represent the primordial building blocks of the comet.

6 ALTERNATIVE INTERPRETATION OF SURFACE BUMPS ON 67P/CG

A pervasive network of fractures covers the surface of Comet 67P/CG where consolidated material is exposed (e.g. Fig. 1a), and intersects to form thermal-contraction crack polygons over ∼1.5 per cent of the surface (El-Maarry et al. 2015b; Auger et al. 2018). Auger et al. (2018) measure the diameters of several thousand polygons using OSIRIS imagery, and find that their characteristic sizes are ∼3.0 ± 1.4 m. They classify the surface bumps observed in the Seth 01 pit (see Auger et al. (2018)'s fig. 8) as 'type 3 and type 4' polygons, which refers to the evolutionary state of the polygon morphology; the older the polygon morphology, the deeper and wider their surrounding troughs (Auger et al. 2018). Type 3 polygons are defined as having relatively rounded surfaces with pronounced troughs, and type 4 polygons are characterized by well-rounded surfaces with the deepest and widest troughs observed on 67P/CG (see Auger et al. (2018)'s fig. 6). Auger et al. (2018) conclude that the surface bumps identified and characterized by Sierks et al. (2015) and Davidsson et al. (2016) are unlikely to be primordial boulders and are consistent with formation of a purely thermal origin – by seasonal contraction and expansion of the sintered icy consolidated material. This hypothesis would explain the lack of signal broadening observed by CONSERT over penetration depths >10 m (Kofman et al. 2015; Ciarletti et al. 2017; Hérique et al. 2019) as well as our estimated limit on the size of primordial building blocks to $\lesssim$ 1 m (see Section 5).

7 USING EARTH-BASED RADAR TO MONITOR THE STRUCTURAL EVOLUTION OF COMET 67P/CG

The next closest approach of Comet 67P/CG will occur in 2021 November at ∼0.4 AU from Earth and presents the next opportunity for Earth-based radar to conduct observations (Farnocchia 2017). The nucleus was only ever observed by Earth-based radar in 1982 from the Arecibo Observatory at the same proximity – the results of which were recently reanalysed after the comet's shape was constrained from optical data that enabled improved estimation of the surface's radar albedo (Kamoun et al. 1982; Kamoun et al. 2014). The 3D post-rendezvous dielectric model presented in this study (Fig. 4), updated using observations by the Rosetta mission, is intended for use by Earth-based radar observations at *X*-band, *S*-band, and *VHF* frequencies – 8.5 GHz (4 cm), 2.4 GHz (13 cm), and ∼10–100 MHz (3–30 m), respectively – to interpret radar reflectivity in terms of 67P/CG's structural evolution.

The major implications of this study pertain to changes in initial assumptions that were accepted in the past by the small-body community when interpreting cometary radar observations. First, unlike asteroids, which have thick, well-gardened regoliths with homogeneous dielectric properties (Palmer et al. 2015), Comet 67P/CG has an actively reworked surface that is dielectrically heterogeneous due to the uneven distribution of regolith material. Roughly 30 per cent of 67P/CG's surface is covered by thick, loose fine-grained deposits (i.e. with blocks < 1 m in diameter) of dust and ice with $\varepsilon_{\mathrm{r}}{}' \lesssim 1.6$–$1.9$, while the remaining 70 per cent consists of exposed consolidated material with $\varepsilon_{\mathrm{r}}{}' \lesssim 2.0$–$3.2$. Secondly, the surface of 67P/CG appears to be rough at *X*- and *S*-band radar wavelength scales for both primary types of surface terrain (Figs 2c and f) and appears rough up to multimetre (VHF wavelength) scales for the consolidated material that covers most of the surface (Figs 2a; 4a–c). Hence, radar observations at *X*- and *S*-band frequencies cannot employ the assumption that the surface is relatively smooth at scales larger than the radar wavelength (i.e. cannot assume the presence of specular reflection) – as this yields inaccurate estimates of the dielectric constant of the surface (Sultan-Salem & Tyler 2006).

With an accurate updated understanding of the radar properties of Comet 67P/CG using the results of the Rosetta mission, we suggest that future Earth-based observations of 67P/CG will be able to interpret radar backscatter in terms of the nucleus' structural evolution. Changes in radar reflectivity, in other words, will indicate changes in the textural and structural properties of the nucleus – such as further fracturing of the exposed consolidated material due to thermal stresses, the collapse of cliffs or jet activity that releases new airfall deposits of fine-grained material, or in the event of the breakup of the bi-lobate comet nucleus that would expose its primordial interior. During the process of surface maturation, for example, fine-grained dust-ice deposits are hypothesized to thicken and increasingly insulate the nucleus surface over time (e.g. Birch et al. 2017; El-Maarry et al. 2017), which would lower the average

dielectric constant of the surface due to increased coverage by loose, low-dielectric material, thereby decreasing radar reflectivity in *X*- and *S*-band radar observations (VHF radar observations would also indicate a darker radar surface reflectivity due to increased surface smoothness on multimetre scales, as a consequence of decreased exposure of the underlying consolidated substrate). Alternatively, increased cometary activity will result in further exposure of consolidated material, leading to an increase in the surface's average dielectric properties, and subsequently brighter radar backscatter reflectivity.

Finally, the above implications are also important to understanding why comet surfaces do not exhibit enhanced radar circular polarization ratios greater than unity like the icy satellites of Jupiter and Saturn. Ostro et al. (2006, 2010) find that due to the mature regoliths on each of Saturn's icy satellites, spatial variations in surface radar reflectivity can be explained by differences in composition rather than surface roughness or volumetric scattering. Comet 67P/CG, in contrast, is still geologically active, and its surface is not covered by a thick regolith layer but fine-grained dust-ice deposits, scattered boulders, and expansive outcrops of rough consolidated material. Hence, the radar reflectivity enhancing effects of volumetric scattering in ice that are observed from comparatively smooth icy satellites are unlikely to apply for 67P/CG at *X*-band or *S*-band frequencies due to intensive scattering at the surface and shallow subsurface. The effect of enhancement may be measurable, however, if high-resolution orbital radar observations at VHF frequencies specifically target fine-grained deposits.

8 CONCLUSIONS

We constructed the post-rendezvous 3D dielectric model of Comet 67P/CG (Fig. 4) accounting for the occurrence of: (1) thick fine-grained dust-ice deposits covering ∼30 per cent of the surface with an estimated relative dielectric constant $\varepsilon_r' \lesssim 1.6$–$1.9$; (2) consolidated material in the underlying substrate that is exposed over ∼70 per cent of the comet surface with $\varepsilon_r' \lesssim 2.0$–$3.2$; and (3) the primordial interior with structural and dielectric homogeneity at metre-scales with $\varepsilon_r' = 1.27 \pm 0.05$ (Kofman et al. 2015). Hence, while on the multimetre scale 67P/CG appears relatively smooth where the surface is coated with thick fine-grained dust-ice deposits (Fig. 2a), at cm-dm scales these surface units are rough, and therefore cannot be treated as sites of specular reflection at *X*- and *S*-band radar observations. This is of particular relevance to the interpretation of the Rosetta RSI *X*- and *S*-band bistatic radar data acquired at 67P/CG, as our results suggest that the dielectric constant of the surface material cannot be inferred from either *X*- or *S*-band radar backscatter observations without radar backscatter simulations, since the signal will be dominated by diffuse backscatter.

We suggest that the bumpy surface texture observed with characteristic diameters of 2.5 ± 1 m (Sierks et al. 2015; Davidsson et al. 2016) are unlikely to be continuous throughout the subsurface, and do not represent the primordial building blocks that formed the comet nucleus. We find that these freshly exposed features observed along the Aswan cliff wall have sufficient dielectric contrast (i.e., likely ≥ 0.15) that if their occurrence is continuous in the subsurface and not only limited to the walls of pits or cliffsides, they would generate measurable broadening in the CONSERT signal due to volume scattering. No such broadening has been observed by CONSERT as shown by Kofman et al. (2015) and Ciarletti et al. (2017) in subsurface volume scattering observations of the nucleus head interior. Alternatively, if the primordial building blocks of the nucleus are preserved in the upper metres of the nucleus, they must be ≤ 1 m in diameter to remove volume scattering and its associated signal in CONSERT radar pulses. We hence conclude that the bumpy surface texture observed along pit and cliff walls are more likely formed by thermal contractions of the icy shallow subsurface.

In all, Comet 67P/CG is the first comet whose dielectric properties have been observed and measured *in situ*, making it a reference for understanding the radar properties of active comets. We suggest that future changes in the Earth-based observed radar reflectivity of the comet nucleus can be associated with large-scale changes in 67P/CG's structural and textural properties. Such changes may indicate increased fine-grained surface deposit coverage and subsequent increase in surface insolation, or increased roughness associated with increased fracturing and thermal weathering of cliff-sides, overhang collapses, and/or nucleus breakup.

ACKNOWLEDGEMENTS

The authors are thankful for the support of Rosetta's Jet Propulsion laboratory (JPL) Project Manager Art Chmielewski, and Project Scientists Dr. Matthew Taylor and Dr. Bonnie Buratti for the discussions that helped generate this manuscript. Palmer is grateful to the University of Southern California for funding. This research is funded under the National Aeronautics and Space Administration (NASA) JPL award to Rosetta Co-Investigator Heggy (005608–00001/Prime No: NNN12AA01C). Kofman and Hérique are funded under Rosetta project funds from Centre National d'Etudes Spatiales (CNES)..

REFERENCES

Auger A.-T. et al. 2018, Icarus, 301, 173
Balsiger H. et al. 2007, Space Sci. Rev., 128, 745
Bardyn A. et al. 2017, MNRAS, 469, S712
Basilevsky A. T., Krasil'nikov S. S., Shiryaev A. A., Mall U., Keller H. U., Skorov Y. V., Mottola S., Hviid S. F. 2016, Solar Sys. Res., 50, 225
Belton M. J. S. et al. 2007, Icarus, 191, 573
Benner L. A. M., 2019, Radar-Detected Asteroids and Comets, Retrieved from https://echo.jpl.nasa.gov/asteroids
Benner L. A. M. et al. 2008, Icarus, 198, 294
Bibring J.-P. et al. 2015, Science, 349, aab0671
Birch S. P. D. et al. 2017, MNRAS, 469, S50
Blum J. et al. 2017, MNRAS, 469, S755
Brouet Y., Levasseur-Regourd A. C., Encrenaz P., Gulkis S. 2014, Planet. Space Sci., 103, 143
Brouet Y. et al. 2016, MNRAS, 462, S89
Brugger B. et al. 2016, ApJ, 822, 98
Capaccioni F. et al. 2015, Science, 347, aaa0628
Carley R. A., Heggy E. 2008, Meteorit. Planet. Sci., 43, 1085
Choukroun M. et al. 2015, A&A, 583, A28
Chýlek P., Ramaswamy V., Srivastava V. 1983, J. Geophys. Res., 88, 10837
Ciarletti V., Levasseur-Regourd A. C., Lasue J., Statz C., Plettemeier D., Hérique A., Rogez Y., Kofman W. 2015, A&A, 583, A40
Ciarletti V. et al. 2017, MNRAS, 469, S805
Ciarniello M. et al. 2016, MNRAS, S443, 462
Dang C., Fu Q., Warren S. G. 2016, J. Atmos. Sci., 73, 3573
Davidsson B. J. R. et al. 2016, A&A, 592, A63
Della Corte V. et al. 2015, A&A, 583, A13
De Sanctis M. C. et al. 2015, Nature, 525, 500
Dobrică E., Engrand C., Leroux H., Rouzaud J.-N., Duprat J. 2012, Geochim. Cosmochim. Acta, 76, 68
El-Maarry M. R. et al. 2015a, A&A, 583, A26
El-Maarry M. R. et al. 2015b, Geophys. Res. Lett., 42, 5170
El-Maarry M. R. et al. 2016, A&A, 593, A110

El-Maarry M. R. et al. 2017, Science, 355, 1392
Farnocchia D., 2017, JPL Small-Body Database Browser: 67P/Churyumov-Gerasimenko, Retrieved from https://ssd.jpl.nasa.gov/sbdb.cgi?sstr=67p
Filacchione G. et al. 2016a, Icarus, 274, 334
Filacchione G. et al. 2016b, Nature, 529, 368
Fornasier S. et al. 2015, A&A, 583, A30
Fornasier S. et al. 2016, Science, 354, 1566
Fulle M. et al. 2017, MNRAS, 469, S45
Fulle M. et al. 2019, MNRAS, 482, 3326
Guilbert-Lepoutre A., Rosenberg E. D., Prialnik D., Besse S. 2016, MNRAS, 462, S146
Gutiérrez P. J. et al. 2016, A&A, 590, A46
Hapke B. 1981, J. Geophys. Res., 86, 3039
Hapke B. 2012, Theory of Reflectance and Emittance Spectroscopy, 2nd ed., Cambridge Univ. Press, New York, NY
Harmon J. K., Nolan M. C., Ostro S. J., Campbell D. B. 2004, in Festou M. C. Keller H. U. Weaver H. A., eds., Comets II, Univ. Arizona Press, Tucson, AZ, 265
Heggy E., Palmer E. M., Kofman W., Clifford S. M., Righter K., Hérique A. 2012, Icarus, 221, 925
Hérique A., Gilchrist J., Kofman W., Klinger J. 2002, Planet. Space Sci., 50, 857
Hérique A., Kofman W., Zine S., Blum J., Vincent J.-B., Ciarletti V. 2019, A&A, in press
Hérique A. et al. 2016, MNRAS, 462, S516
Israelachvili J. N. 2011, Intermolecular and Surface Forces, 3rd ed., Acad. Press, Burlington, MA
Jorda L. et al. 2016, Icarus, 277, 257
Kamoun P., Lamy P. L., Toth I., Herique A. 2014, A&A, 568, A21
Kamoun P. G., Campbell D. B., Ostro S. J., Pettengill G. H., Shapiro I. I. 1982, Science, 216, 293
Keller H. U. et al. 2007, Space Sci. Rev., 128, 433
Kieffer H. H. 1990, J. Geophys. Res., 95, 1481
Kiuchi M., Nakamura A. M. 2014, Icarus, 239, 291
Kofman W. et al. 1998, Adv. Space Res., 21, 1589
Kofman W. et al. 2015, Science, 349, aab0639
Kossacki K. J., Spohn T., Hagermann A., Kaufmann E., Kührt E. 2015, Icarus, 260, 464
Kossacki K. J., Szutowicz S. 2008, Icarus, 195, 705
Lamy P. L., Herique A., Toth I. 2015, Space Sci. Rev., 197, 85
Lethuillier A. et al. 2016, A&A, 591, A32
Liou K. N., Takano Y., He C., Yang P., Leung L. R., Gu Y., Lee W. L. 2014, J. Geophys. Res. Atmos., 119, 7616
Massironi M. et al. 2015, Nature, 526, 402
Mottola S. et al. 2015, Science, 349, aab0232
Nunes D. C., Phillips R. J. 2006, J. Geophys. Res., 111
Oklay N. et al. 2017, MNRAS, 469, S582
Ostro S. J. et al. 2006, Icarus, 183, 479
Ostro S. J. et al. 2010, Icarus, 206, 498
Pajola M. et al. 2017, Nat. Astron., 1, 0092
Palmer E. M., Heggy E., Capria M. T., Tosi F. 2015, Icarus, 262, 93
Palmer E. M., Heggy E., Kofman W. 2017, Nat. Commun., 8, 1
Pommerol A. et al. 2015, A&A, 583, A25
Preusker F. et al. 2015, A&A, 583, A33
Prialnik D., Sierks H. 2017, MNRAS, 469, S217
Pätzold M. et al. 2007, Space Sci. Rev., 128, 599
Pätzold M. et al. 2016, Nature, 530, 63
Pätzold M. et al. 2019, MNRAS, 483, 2337
Quirico E. et al. 2016, Icarus, 272, 32
Rosenberg E. D., Prialnik D. 2009, Icarus, 201, 740
Rotundi A. et al. 2015, Science, 347, aaa3905
Sierks H. et al. 2015, Science, 347, aaa1044
Sihvola A. H. 1999, Electromagnetic Mixing Formulas and Applications, IEE Publishing, London, UK
Spohn T. et al. 2015, Science, 349, aab0464
Springmann A. et al. 2017, in AAS/DPS Meeting Abstracts, Particle Sizes in the Coma of Comet 45P/Honda-Mrkos-Pajdušáková from Arecibo Radar Observations, Vol. 49, American Astronomical Society, Washington, p. 305.
Sultan-Salem A. K., Tyler G. L. 2006, J. Geophys. Res., 111, E06S07
Thomas N. et al. 2015, A&A, 583, A17
Tosi F. et al. 2015, Lunar Planet. Sci. Conf., 46, Abstract #2156, Lunar and Planetary Institute, Houston, TX
Vincent J.-B. et al. 2015, Nature, 523, 63
Virkki A., Muinonen K. 2016, Icarus, 269, 38
von Hippel A. R. , 1995, Dielectric materials and applications. Artech House. Boston, MA
Warren S. G. 1982, Rev. Geophys. Space Phys., 20, 67
Wright I. P. et al. 2007, Space Sci. Rev., 128, 363
Yoldi Z., Pommerol A., Jost B., Poch O., Gouman J., Thomas N. 2015, Geophys. Res. Lett., 42, 6205

SUPPORTING INFORMATION

Supplementary data are available at *MNRAS* online.

Figure A1. Albedo of a dust-ice mixture versus dust mass fraction for different effective grain size ratios between the dust and ice particles.

Figure A2. Same as Fig. A1 but with a larger dust effective grain size of 200 μm.

Please note: Oxford University Press is not responsible for the content or functionality of any supporting materials supplied by the authors. Any queries (other than missing material) should be directed to the corresponding author for the article.

This paper has been typeset from a TEX/LATEX file prepared by the author.